Perspective

# Advancements and Applications of Conjugated Polyelectrolytes and Conjugated Oligoelectrolytes in Bioanalytical and Electrochemical Contexts

Sarah J. Cox-Vázquez, Batul Shakir, Oscar Medrano, Dhari Shah, Kingsley Bortey, Bidisha Biswas, Austin Tran, Crystal Tran, and Ricardo Javier Vázquez*

Read Online

ACCESS | Metrics & More | Article Recommendations

**ABSTRACT:** In the past decade, conjugated oligoelectrolytes (COEs) and conjugated polyelectrolytes (CPEs) have emerged at the forefront of active materials in bioanalytical and electrochemical settings due to their unique electronic and ionic properties. These materials possess $\pi$-conjugated backbones with ionic functionalities at the ends of their side chains, granting them water solubility and facilitating their processability, exploration, and applications in aqueous environments. In this perspective, the basis for evaluating their figures of merit in selected bioanalytical and electrochemical contexts will be provided and contextualized. We will primarily discuss their roles in biosensing, bioimaging, bioelectrosynthesis, and electrochemical contexts, such as organic electrochemical transistors (OECTs), microbial fuel cells (MFCs), and their use as charge-storing materials. Emphasis will be placed on their role in improving efficiency and utility within these applications. We will also explore the fundamental mechanisms that govern their behavior and highlight innovative strategies and perspectives for developing the next generation of CPEs and COEs for bioanalytical and electrochemical applications and their integration into practical devices.

Membrane-Intercalating Conjugated Oligoelectrolytes (COE) — Self-Doped Conjugated polyelectrolytes (CPE)
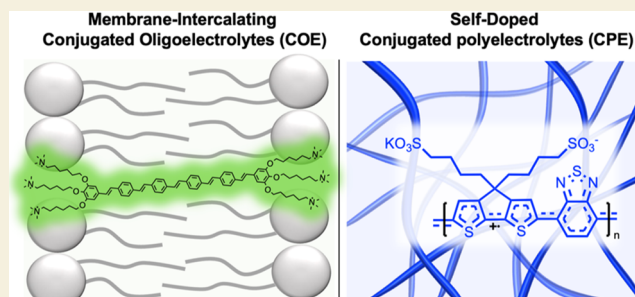
## 1. INTRODUCTION

The synthetic flexibility of organic semiconductors (OSCs) has positioned them at the forefront of technological advancements in various fields, including but not limited to photovoltaics,[1−4] light-emitting diodes,[5−8] electrochemical transistors,[9,10] neuromorphic computers,[11,12] bioanalytics,[13−15] and electrochemical energy storage.[16,17] The main optoelectronic advantage of OSCs comes from their tunable $\pi$-conjugated backbones.[1] In addition to their tunable properties through molecular design, these materials also benefit from being lightweight, mechanically flexible, easy to process, and cost-effective.

A breakthrough in the OSC field was achieved when ionic functionalities were incorporated into their $\pi$-conjugated backbones, granting them water solubility for exploring applications in aqueous environments.[18−21] These materials are often referred to as conjugated oligoelectrolytes (COEs) and conjugated polyelectrolytes (CPEs), see Figure 1. They combine the unique optoelectrical properties of OSCs with the ability to modulate their physical properties through side chain electrostatic engineering.[22−24] COEs are often associated with

conjugated small molecules with a finite number of repeating conjugated units (n) < 8, while CPEs are often associated with conjugated polymers with $n > 8$.[25]

The key physical property of COEs is their ability to spontaneously intercalate into the lipid bilayer in biological membranes, enabling an unprecedented membrane-material interface for antimicrobial,[26] biosensing,[14] bioimaging,[27] and bioelectrosynthesis applications.[28] Note that the COE's total length is important for its biocompatibility within the membrane, as shorter COEs (<3 nm) show greater toxicity than longer COEs (>4 nm).[26] Other water-soluble conjugated small molecules with similar applications exist,[29−31] but COEs are the only materials that can span the entire lipid bilayer. We
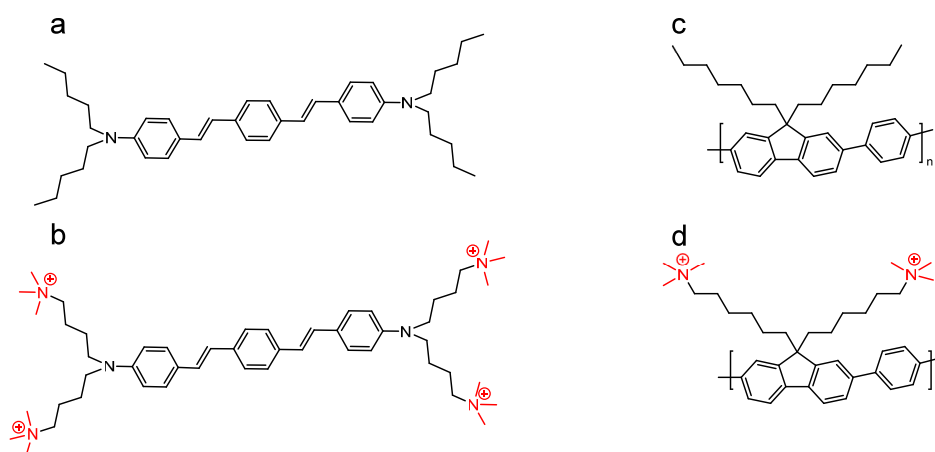
**Figure 1.** (a) The molecular structure of an archetypical small molecule OSC and (b) its COE congener. (c) The molecular structure of an archetypical OSC polymer, or conjugated polymer, and (d) its CPE congener.
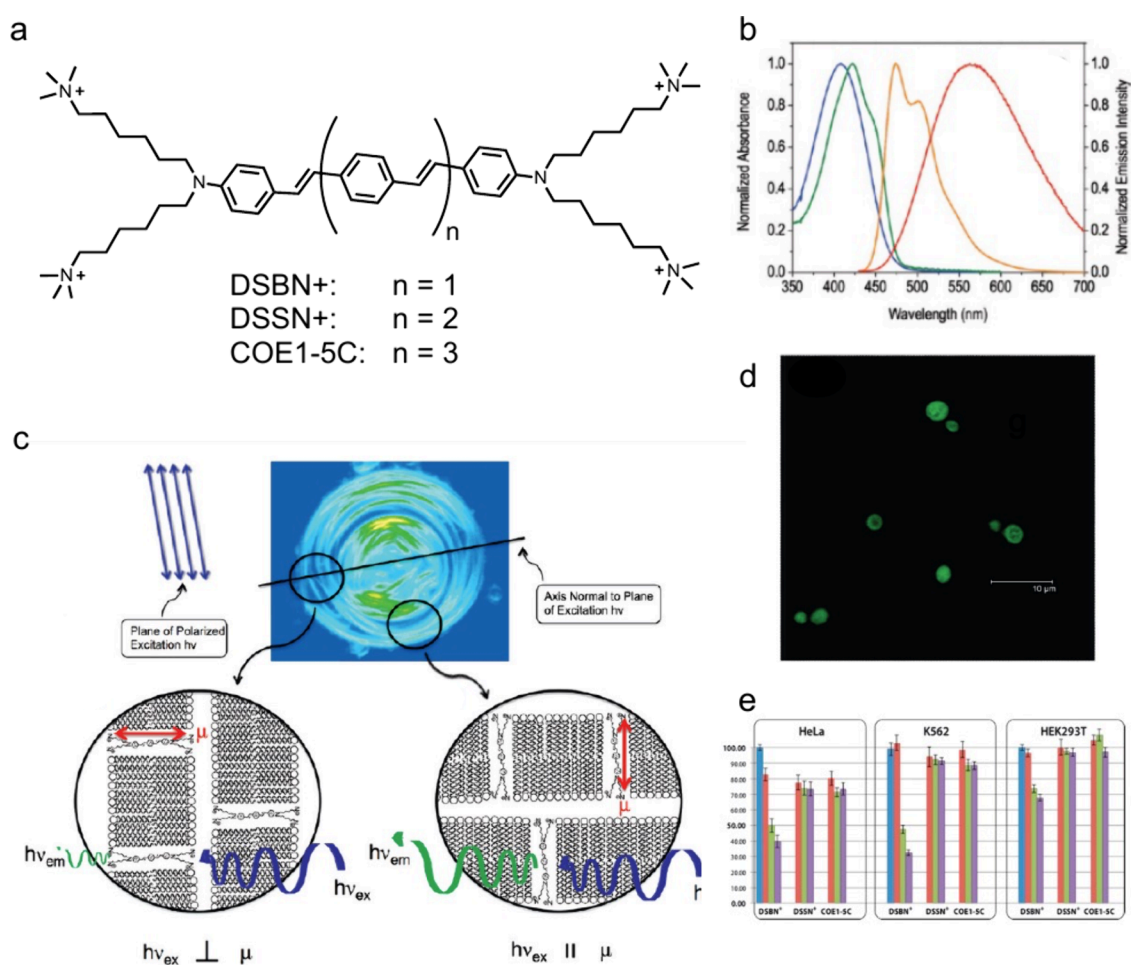


**Figure 2.** (a) Molecular structures of COEs with 4 ionic pendant groups. (b) Normalized absorption and emission spectra of DSBN+ in buffer "absorbance = blue, emission = red" and while embedded within lipid vesicle membranes "absorbance = green, emission = orange". (c) Fluorescence micrograph of large multilamellar vesicle containing 3 mol % of DSBN+ that exhibits an equatorial extinction line "black line" perpendicular to the plane of excitation light and schematic representing the orientation of DSBN+ in the lipid bilayer. (d) Confocal microscopy fluorescence images of Baker's yeast stained with 100 $\mu$M DSBN+. Adapted with permission.[49] Copyright 2010, ACS. (e) Viability of human cell lines after 48 h of incubation with DSSN+, DSBN+, and COE1-5C; control "blue", 1 $\mu$M "red", 10 $\mu$M "green", and 20 $\mu$M "purple". Adapted with permission.[51] Copyright 2014, RSC.

direct the reader to a recent review by Yong and co-workers for a detailed tutorial review of COEs.[26]

The key physical property of CPEs is that their dopability, mechanical, and opto-electrochemical properties are linked to the presence of ionic groups on the side chains, and can be
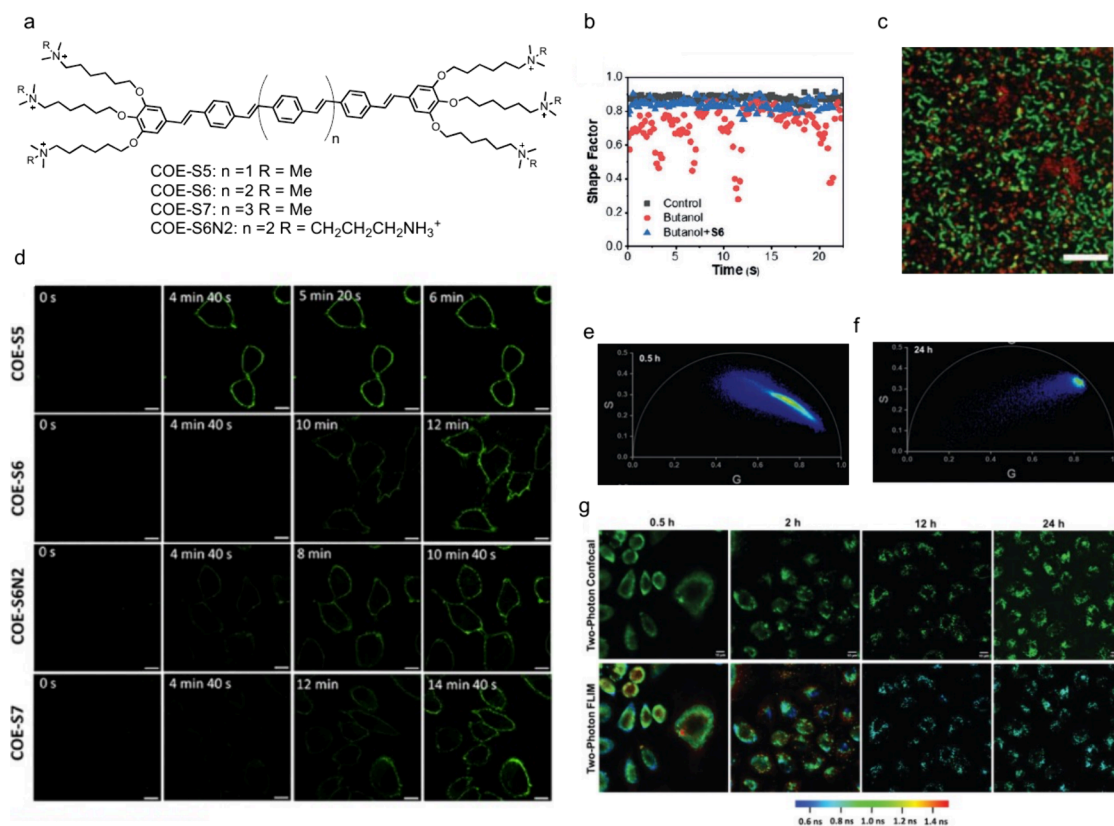
**Figure 3.** (a) Molecular structure of elongated COEs with 6 ionic pendant groups. (b) The shape factor of GUVs with and without COE-S6 after the addition of butanol. Adapted with permission.[53] Copyright 2019, Wiley-VCH. (c) Confocal microscopy image of a biofilm shows selective staining of *S. aureus* with COE-S6 "green" and FM 4−64 staining *P. aeruginosa* in "red". Adapted with permission.[54] Copyright 2020, Wiley-VCH. (d) Timelapse confocal microscopy of membrane intercalation of COEs into A549 cells. Adapted with permission.[55] Copyright 2023 Cell Press. Phasor plot after (e) 0.5 h and (f) 24 h of incubation of COE-S6 with A549 cells, and (g) Confocal and FLIM images showing the time course of intercalation with the color indicating the lifetime at the individual pixel. Adapted with permission.[56] Copyright 2023, Wiley-VCH.

modulated by external stimuli, such as ionic content and identity.[32−35] Water-soluble conjugated polymers containing nonionic ethylene glycol side chains have been reported.[36−39] This group of OSCs is referred to as organic mixed ion-electron conductors (OMIECs) when adapted into transistor devices, and can also exhibit some of the bioanalytical and electrochemical properties characteristic of CPEs, such as ion-electron signal amplification and electrochemical energy storage.[40−43] OMIECs will be discussed and contextualized here where appropriate. However, OMIECs typically lack certain properties that CPEs possess, such as self-doping activity triggered by pH changes and ion-induced Coulombic cross-linking.[44] We direct the reader to a recent review by Rivnay and co-workers for a detailed tutorial review on OMIECs.[45]

## 2. COES IN A BIOANALYTICAL CONTEXT

### 2.1. Fundamentals of COEs in Bioanalysis

The main figures of merit for COEs when interfacing with biology are their molar absorptivity ($\varepsilon$), quantum yield ($\Phi$), brightness, fluorogenicity, and fluorescence lifetime ($\tau$).[13,46,47] The $\varepsilon$ is the molecule's ability to absorb photons, as described by Beer−Lambert law.[2] The quantum yield ($\Phi$) is the ratio of emitted photons to absorbed ones and is often determined using the Williams' direct comparison method with a fluorophore standard that has a known $\Phi$, such as Rhodamine B or Fluorescein.[5] Brightness is determined by multiplying $\varepsilon$ by

$\Phi$, and higher brightness is desired when using emission as an optical reporter in bioanalysis. Fluorogenicity refers to the molecule's ability to transition from a less-emissive state (lower $\Phi$) to a more-emissive state (higher $\Phi$) in response to an external stimulus, such as membrane intercalation.[48] The $\tau$ is the time a molecule remains in its excited state before relaxing to the ground state, which is unique to the molecule but can be influenced by the molecule's surroundings.[13] The following section of the perspective will focus on the development of COEs for bioanalysis, whose fluorescent properties can serve as analytical signals for detecting large biomolecules of interest based on the principles discussed above. Particular attention is given to innovations in molecular design that have expanded the application of COEs, along with insights into their structure−function relationships that are relevant to this field.

### 2.2. COEs as Membrane Intercalating Optical Reporters

In 2010, the Bazan group described the membrane intercalation of two COEs, DSBN+ and DSSN+ (Figure 2a).[49] The structure of these COEs was unique compared to their predecessors, as the ionic pendant groups on the new COEs are "wings" on each side of the conjugated core instead of being attached along the backbone.[50] This molecular architecture of DSSN+ and DSBN+, presumably, mimicked the amphipathic domains of lipids oriented in a bilayer. Photophysical evidence such as redshift in absorbance and blue shift in the emission of the COEs was obtained after intercalation into the lipid bilayer of unilamellar and
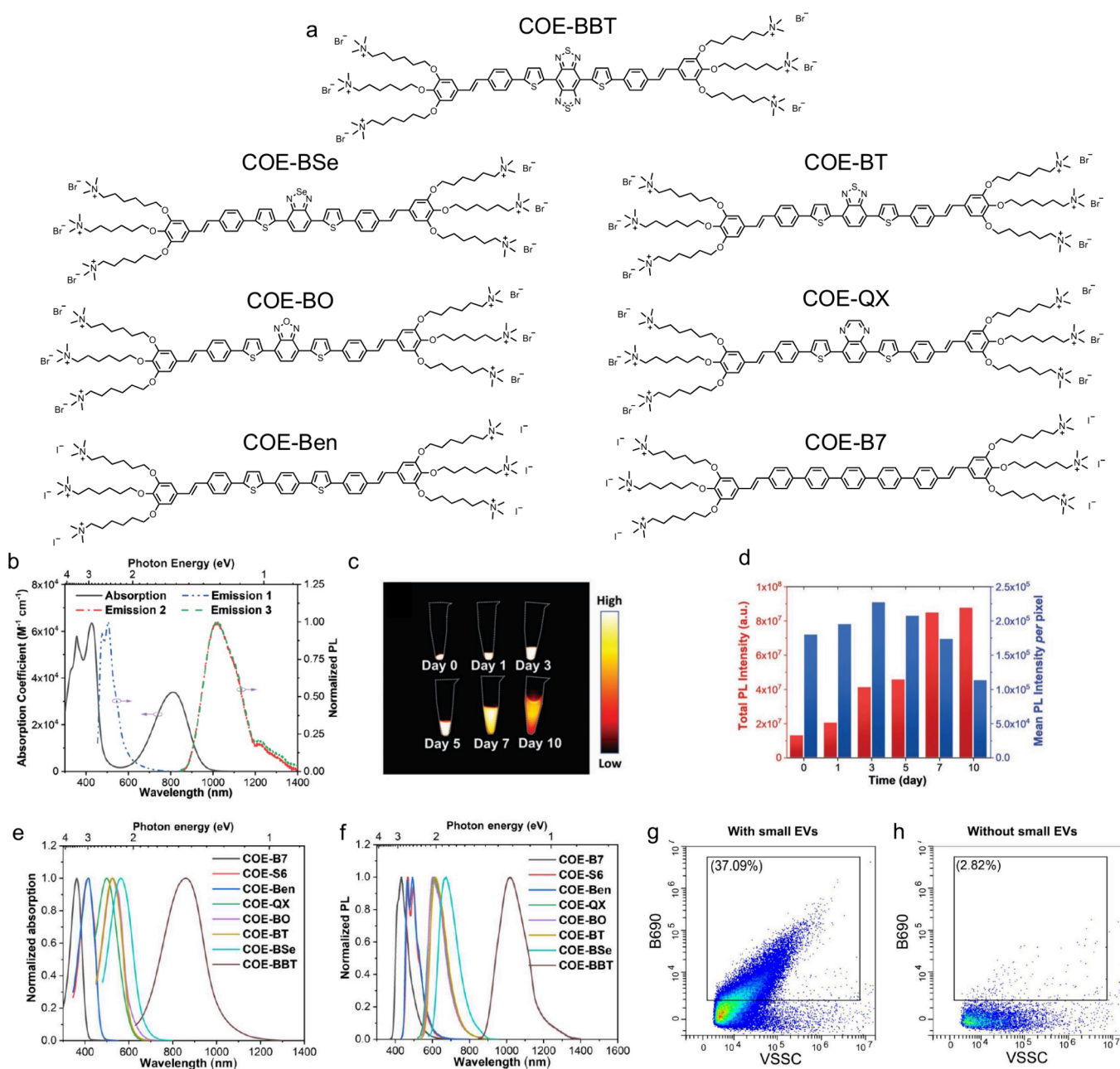
**Figure 4.** (a) Molecular structures of D−A−D COEs with 6 ionic pendant groups. (b) Absorption and emission spectra of COE-BBT, (c) NIR-II image of the extracted tumor, and (d) comparison of total image vs per pixel intensity. Adapted with permission.[27] Copyright 2022, Wiley-VCH. Normalized (e) absorption and (f) emission spectra of the of D−A−D COEs. Flow cytometry plots of small EVs stained with (g) COE-BT and (h) the dye alone showing no aggregation that can convolute with the stained EVs analytical signals. Adapted with permission.[14] Copyright 2023, AAAS.

multilamellar vesicles, attributed to the difference in polarity between water and lipids (Figure 2b). Notably, confirmation that the orientation of the COEs within the bilayer was in parallel alignment with the lipids was obtained using polarized fluorescence microscopy, indicating that the charged amines interact with the head groups of the phospholipids. The conjugated core is inserted into the hydrophobic region of the bilayer, spanning the entire bilayer (Figure 2c). It was also confirmed that DSSN+ and DSBN+ could spontaneously intercalate into live cell membranes of yeast (Figure 2d).

Following this work, in 2014, Gwozdzinska et al. demonstrated using DSBN+, DSSN+, and COE1-5C as stains for mammalian cell membranes in fluorescent microscopy.[51]

Notably, this work emphasized the low to moderate toxicity levels of COEs and their ability to penetrate cells and stain various membranous structures, including the Golgi and endoplasmic reticulum, efficiently of multiple cell culture lines, including HeLa, K652 and HEK-293T. DSSN+ and COE1-5C exhibited low toxicity levels, while DSBN+, the shortest COE tested, showed moderate toxicity at 10 or 20 $\mu$M in all cell lines (Figure 2e), demonstrating that the overall length from charge to charge is important for its biocompatibility. In 2015, Czernek et al. used DSSN+ to stain extracellular vesicles (EVs) derived from cancer cells.[52] DSSN+ was used to stain the EVs to track their uptake into

**Table 1. Summary of the Photophysical Properties of COEs for Bioanalytical Assays[a]**

| | Analyte | $\Phi$ (%) | $\varepsilon$ ($10^4$ $M^{-1}$ $cm^{-1}$) | $\lambda_{abs}$ | $\lambda_{em}$ |
|---|---|---|---|---|---|
| DSBN+[49,51,74] | lipid bilayer | 33[b], 59[d] | 6.0 | 406[b] | 566[b] 474[d] |
| DSSN+[49,51,52,74] | lipid bilayer | 6[b], 85[d] | 6.6 | 412[b] | 594[b] 532[d] |
| COE1-5C[51,53] | lipid bilayer | n/a | 9.30 | 430[b] | 574 |
| COE-S5[55] | lipid bilayer | 20[b], 92[c] | 9.30 | 398[b] | 507[b] |
| COE-S6[14,53,54,56] | lipid bilayer | 16[b], 89[c], 70[d] | 9.70 | 408[b] | 520[b] 467[d] |
| COE-S6N2[55] | lipid bilayer | 15[b], 77[c] | 9.40 | 408[b] | 519[b] |
| COE-S7[55] | lipid bilayer | 1[b], 76[c] | 11.1 | 416[b] | 530[b] |
| COE-Ben[14] | lipid bilayer | 60[d] | 7.00 | 410[b] | 492[d] |
| COE-BT[14] | lipid bilayer | 25[d] | 2.60 | 527[b] | 614[d] |
| COE-B7[14] | lipid bilayer | 94[d] | 9.80 | 365[b] | 434[d] |
| COE-BO[14] | lipid bilayer | 27[d] | 3.00 | 536[b] | 601[d] |
| COE-BSe[14] | lipid bilayer | 9.2[d] | 2.2 | 563[b] | 674[d] |
| COE-QX[14] | lipid bilayer | 23[d] | 2.6 | 499[b] | 609[d] |
| COE-BBT[14,27] | lipid bilayer | 0.8[d] | 1.90 | 400[b] 836[b] | 500[b] 1017[b] |
| COE-CN[75] | mitochondria | 35[d] | 1.48 | 392[b] 435[d] | 525[b] 507[d] |
| OPE1−[64,65] | amyloid | n/a | n/a | 380[b] 393[e] | 473[b] 452[e] |
| OPE2+[64,65] | amyloid | n/a | n/a | 402[b] 412[e] | 474[b] 455[e] |

[a]Analyte = species that molecule was responding to in the bioassay. $\Phi$ = quantum yield. $\varepsilon$ = molar absorptivity. $\lambda_{abs}$ = Absorbance maximum. $\lambda_{em}$ = emission maximum. $n/a$ = not available. [b]Measurements were taken in $H_2O$ or PBS. [c]Measurements were taken in methanol. [d]Measurements were taken in lipid bilayers. [e]Measurements were taken in amyloid fibers.

four differentiated myeloid cell types using flow cytometry and fluorescence microscopy.

In 2019, Bazan and co-workers reported COE-S6 (Figure 3a), a backbone-elongated COE with six phenylenevinylene repeating subunits and six ionic pendant groups.[53] COE-S6 demonstrated spontaneous intercalation and localization into the lipid bilayer of bacteria and liposome models owing to its linear and bilayer-mimicking topology, as revealed by fluorescence microscopy and differential scanning calorimetry (DSC) measurements. COE-S6 was more water-soluble than previous iterations of COEs, owing to the increased number of charged side chains. Direct comparison with a shorter and less charged COE, namely COE1-5C, revealed that COE-S6 serves as a hydrophobic support for glycerophospholipid acyl chains, offering better protection to the membrane against butanol-induced toxicity and instability. Moreover, a study of *E. coli* treated with COE-S6 displayed a 2-fold increased tolerance to butanol concentrations from 0.9% to 1.8%. The protective response of COE-S6 against membrane disruption was also validated by real-time fluorescence imaging in giant unilamellar vesicles (GUV) model systems (Figure 3b), in which the shape factor was maintained in GUVs stained with COE-S6 after the addition of butanol but unstained GUVs were unstable as demonstrated by the changing shape factor.

A follow-up study from the same group further employed COE-S6 as an optical tool for distinguishing Gram-types of bacteria in a single step.[54] COE-S6 accumulated in the cell membrane of Gram-positive bacteria, *S. aureus*, instantaneously, showing distinct emission patterns from the membrane boundary in contrast to the Gram-negative bacteria, *P. aeruginosa*, where partitioning into the membrane was minimal. The hindered intercalation of COE-S6 into the Gram-negative bacterial membrane was attributed to the presence of lipopolysaccharide (LPS) in the outer layer of the membrane inhibiting the intercalation, which was determined using large multilamellar vesicles (LMVs) with and without LPS. Moreover, differentiation of the Gram-types was also accomplished in situ within mixed bacterial biofilms by discrete labeling of *S.*

*aureus* with COE-S6 in combination with the nonspecific membrane dye FM 4−64 staining *P. aeruginosa* (Figure 3c).

Zhu et al. investigated the effects of varying phenylene-vinylene subunits (length) and the amounts of quaternized amines (charges) on the membrane-intercalating properties of the elongated COEs into mammalian cells (Figure 3a).[55] As shown in Figure 3d, COE-S5, which is the shortest, stained the A549 cells the quickest. However, over time, the longer COEs and those with more positive charges were found to give a brighter signal (Figure 3d). Quantitative characterization revealed that COEs of longer lengths were better able to integrate themselves into cell membranes, with COE-S7 having a cellular uptake of 81% ± 2% in cells compared to COE-S5′s cellular uptake of 47% ± 2%. Regarding structural orientation, it was further confirmed with polarized fluorescence micros-copy that COEs align themselves perpendicular to the lipid bilayer despite their enhanced water solubility.

Expanding beyond emission intensity, the fluorescence lifetime of a dye can also be used as an optical reporter.[13] Using COE-S6, Zhu et al. investigated its fluorescence lifetime using Two-Photon Fluorescence-Lifetime Imaging Microscopy (FLIM).[56] Using FLIM, a change in the lifetime upon membrane intercalation and endocytosis could be monitored when COE-S6 was incubated with A549 cells. As intercalation and endocytosis progressed from 0.5, 2, 12, and 24 h, the dominant lifetime of COE-S6 changed from $\tau_w$ 1.0 to 0.8 ns, which can be visualized using the phasor plots shown in Figure 3e and Figure 3f. Note that $\tau_w$ is a weighted average of the $\tau$ when there are multiple decay components. The authors attribute this $\tau$ change to the fact that COE-S6 first loosely aggregates on the surface of the lipid bilayer through ionic interactions and then intercalates into the bilayer driven by the hydrophobic effect from its conjugated core, which can be seen in the FLIM images as COE-S6 changes from red (long $\tau$) on the perimeter of the cell, to blue (short $\tau$) and fully internalized over 24 h (Figure 3g). This transition was also reflected in the shift of emission characteristics and the emergence of vibronic features in the fluorescence spectra.
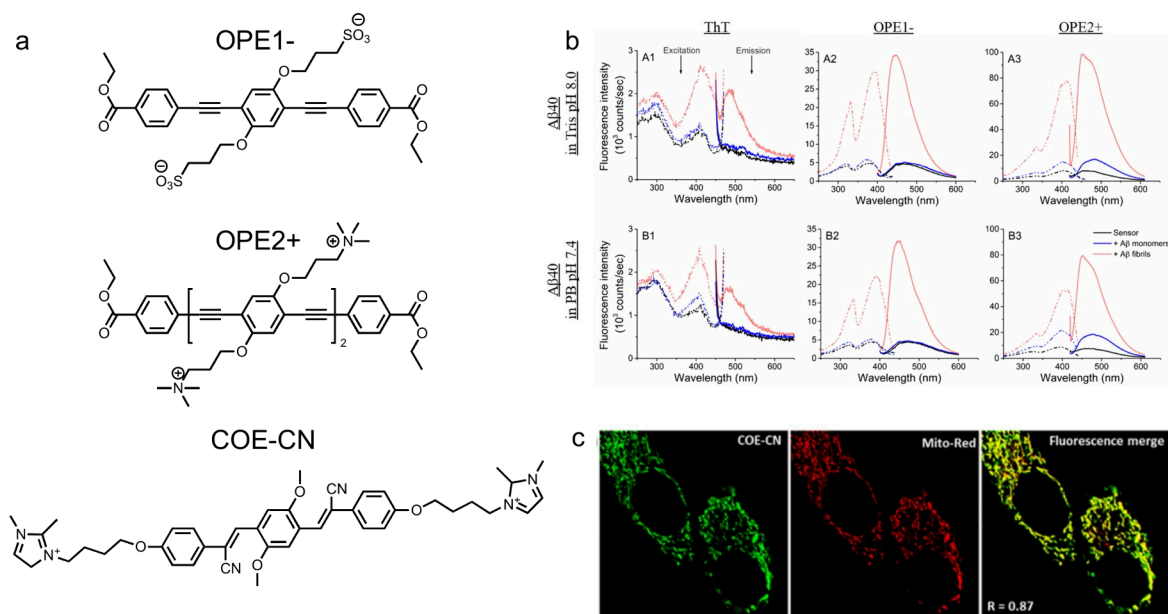
**Figure 5.** (a) Molecular structures of COE derivatives for organelle and protein staining: OPE1−, OPE2+, and COE-CN. (b) Excitation and emission spectra of Thioflavin T (ThT), OPE1− and OPE2+ alone "black" and with Amyloid-beta monomers "blue" or fibers "red" in two different buffers. Adapted with permission.[64] Copyright 2019, ACS. (c) Confocal microscopy image of COE-CN colocalized with commercial mitochondria dye, $R^2$ = 0.87. Adapted with permission.[68] Copyright 2024, ACS.

Bazan and co-workers synthesized a derivative of COE-S6, COE-BBT, with a donor−acceptor−donor (D−A−D) backbone, effectively tunning the emission of the COE to the NIR-II (Figure 4a).[27] Interestingly, COE-BBT displayed two distinct emission bands, one in the visible range at 500 nm and one in the NIR-II range at 1020 nm, see Figure 4b. Showing two emission peaks is unusual, but characteristic of anti-Kasha's behavior.[57] The unique dual emissive property of COE-BBT was explored for accessing distinct excitation channels appropriate for two different imaging techniques, namely confocal microscopy and live animal imaging. The NIR-II emission characteristics of COE-BBT were beneficial for the noninvasive tracking of intracranial and subcutaneous tumors in mouse models. Interestingly, the emission intensity of the tumor stained with COE-BBT increased as the tumor grew over 26 days. This phenomenon was attributed to self-quenching due to the high dye concentration in the bilayer but diluted through cell divisions, showing a high degree of retention and stability in the cells. This hypothesis was validated upon extraction of tumors at different time points, revealing that the mean emission intensity per pixel decreased while the total emission intensity of the sample increased (Figure 4c and Figure 4d).

The same group presented a new series of fluorogenic COEs for detecting and tracking small EVs.[14] Six new COE-S6 derivatives were synthesized with the same phenylenevinylene backbone and varying strength of the D−A−D subunits (Figure 4a), a design that is known to be effective for modulating the absorption (Figure 4e) and emission (Figure 4f) profiles of dyes, see Table 1. For example, the most blue-shifted compound, COE-B7, featured a pentaphenylene sequence with absorbance and emission maxima at 365 and 434 nm, respectively. In contrast, the most red-shifted compound, COE-BSe, employed a benzoselenadiazole unit, resulting in peak absorbance at 569 nm and emission at 674 nm. Achieving color tunability is of academic and commercial interest due to the expansion of instrumentation offerings.

Notably, the COEs showed high water solubility, making them suitable for labeling EVs without laborious free dye removal (Figure 4g and Figure 4h) and multiplexing with other dyes, ultimately removing the false positives seen with traditional membrane dyes.

## 2.3. Perspectives on COE as Membrane Intercalating Optical Reporters

The previous section highlighted significant milestones in developing COEs with unprecedented molecular structure and photophysical properties for the biophysical interrogation of lipid bilayers see Table 1. A key chemical design principle contributing to their success in nontoxic membrane intercalation is the increased length of COEs, which matches that of the lipid bilayer (~5 nm), along with the orientation of charge groups at the terminal ends of the linear, hydrophobic, conjugated emissive molecules. This design allows COEs to align parallel with the individual lipids, making them the only known dye that spans the entirety of the lipid bilayer. This bilayer-spanning capability contributes to membrane stabilization, while shorter COEs can act as membrane disruptors and have been explored for use in antibiotics.[58] The current thinking is that opportunities to develop COEs sensitive to membrane microdomains, such as lipid rafts, and functionalities for measuring membrane dipoles are desirable to increase their utility. Additionally, COEs capable of sensing and reporting ions like $Ca^{2+}$, $Na^{+}$, or $H^{+}$, as well as lipid modifications such as acyl tail oxidation, are needed to develop new tools for understanding specific phenotypes or drug effects.[59−61]

## 2.4. COEs for Protein and Organelle Detection Assays

Amyloid protein deposits are highly implicated in pathologies of neurodegenerative diseases, including Alzheimer's and Parkinson's.[62,63] The smaller size of COEs is particularly advantageous for amyloid detection, which allows them to interact effectively with the repetitive domains of amyloid fibers. This interaction is driven by the hydrophobic
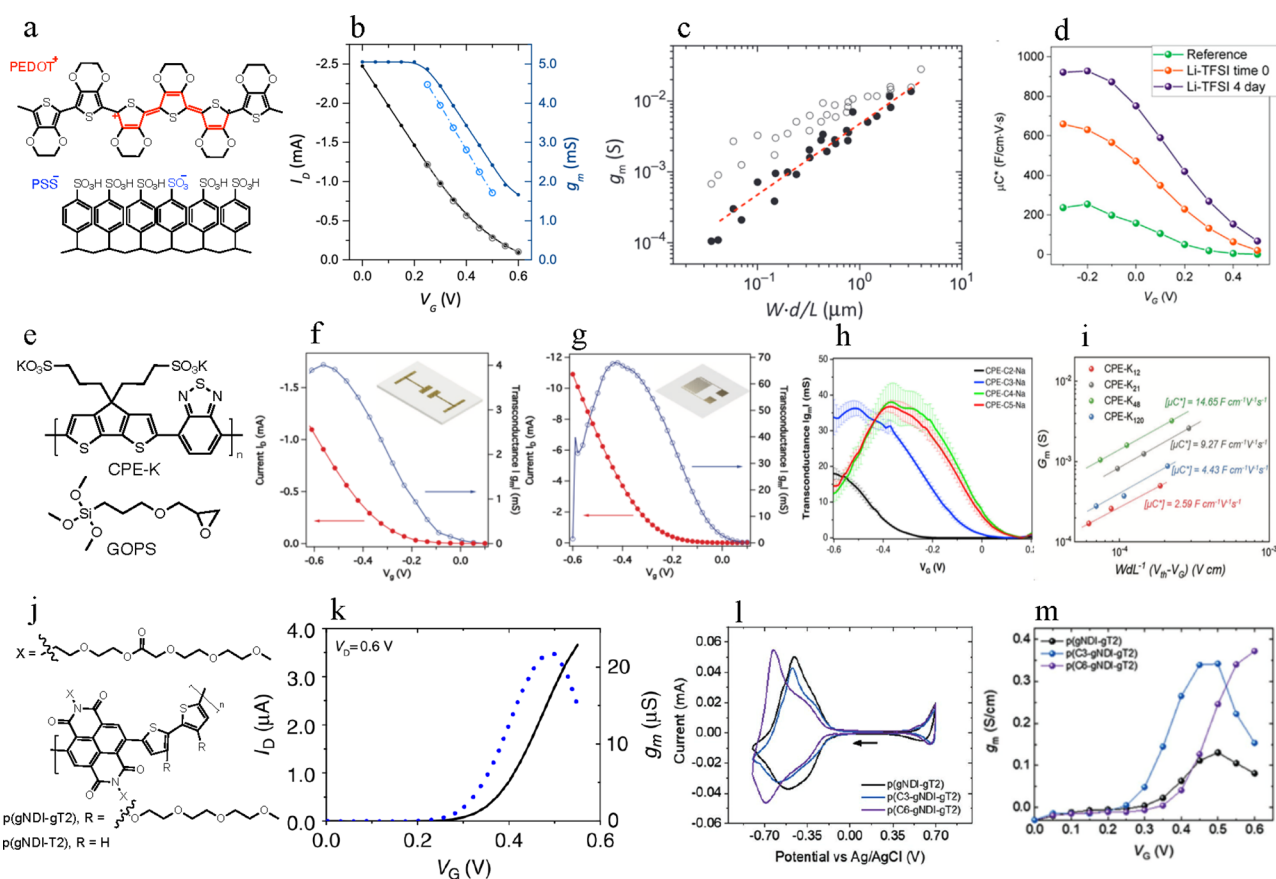
**Figure 6.** (a) The molecular structure of PEDOT:PSS, (b) its transconductance, and (c) the transconductance scalability with thickness. Adapted with permission.[80] Copyright 2015, AAAS. (d) PEDOT:PSS extracted product capacitance as a function of $V_G$ at $V_D = 0.6$ V. Adapted with permission.[90] Copyright 2023, Elsevier Inc. (e) The molecular structure of CPE-K and its initial transconductance values in (f) traditional and (g) interdigitated electrodes. Adapted with permission.[42] Copyright 2020, Wiley-VCH. (h) CPE-K's transconductance as a function of side chain length. Adapted with permission.[91] Copyright 2023, RSC. (i) The impact of the molecular weight of CPE-K on its product capacitance. Adapted with permission.[43] Copyright 2024, Wiley-VCH. (j) The molecular backbone of the discussed NDI-containing OMIECs and (k) the transconductance of p(gNDI-gT2). Adapted with permission.[94] Copyright 2016, Springer Nature. (l) Redox potential and (m) transconductance of p(gNDI-gT2), p(C3-gNDI-gT2), and p(C6-gNDI-gT2). Adapted with permission.[96] Copyright 2021, Wiley-VCH.

amyloidogenic core of many aggregating proteins and the presence of numerous charged residues that provide specific sites for COE interaction. For example, in 2019, Fanni et al. demonstrated that anionic and cationic COEs, OPE1−, and OPE2+, respectively (Figure 5a), showed sensitivity and selectivity in detecting amyloid fibers over monomers.[64] Both COEs were weakly emissive in the buffer, but their emission intensities increased, accompanied by hypochromic shifts, when interacting with amyloid fibers (Figure 5b). Notably, both COEs could detect the formation of aggregates earlier than Thioflavin-T, which is the "gold standard" of amyloid-detecting dyes in *in vitro* and *in vivo* assays, and could detect fiber concentrations as low as 0.24 μM. While Fanni and colleagues were unable to determine the exact binding mechanism of COEs to the fibers, they hypothesized that the planar structures of the fibers induce backbone planarization, leading to emission enhancement in the COEs. Following this work, in 2023, Monge et al. used OPE1− and OPE2+ to stain brain tissue sections from transgenic mouse and rat models of AD and human post-mortem sections diagnosed with frontotemporal dementia.[65] They demonstrated that the COEs could stain plaques in tissue with limited nonspecific staining, as confirmed by immunohistochemistry.

COEs are also well-suited for intracellular organelle detection. Contrarily to their COE congeners, their small size allows for easy diffusion into cells, and specific organelle targeting can be achieved by incorporating particular chemical modifications.[26] Mitochondria are of particular importance because their dysfunction is implicated in a wide range of diseases, including autoimmune diseases, cancer, and neuro-degeneration.[66,67] In 2024, Chan et al. reported COE-CN, which has subcellular targeting to the mitochondria (Figure 5a).[68] Structurally, COE-CN consists of imidazolium solubilizing groups and a luminescent cyanovinyl-associated distyr-ylbenzene framework with intramolecular charge-transfer properties. Colocalization assays performed with COE-CN alongside various organelle-specific dyes indicated a prefer-ential internalization of COE-CN in mitochondria (Figure 5c). Additionally, mitochondria-specific visualization of treated cells using COE-CN under live, fixed, healthy, and depolarized cell conditions established this COE as a versatile dye for cell imaging. COE-CN's emission intensity was found to correlate with mitochondrial health, which was then used to screen healthy versus unhealthy populations with mitochondrial dysfunction via flow cytometry.

**Table 2. Summary of the Optimal OECT Performances for the Selected OMIECs[a]**

| OMIECs | $g_m$ | $\mu C^*$ | $C^*$ | $\mu$ | Device Architecture (W, L) |
|---|---|---|---|---|---|
| p-type CPEs | | | | | |
| PEDOT:PSS[80] | 5 ms | n/a | 39 F/cm³ | 3.8 cm²/(V s) | Planar/Horizontal (50 μm, 50 μm) |
| PEDOT:PSS[90] | 31.4 mS | 752.5 F/cm·V·s | n/a | 9.1 cm²/(V s) | Planar/Horizontal (400 μm, 50 μm) |
| CPE-K[42] | 70 mS | n/a | 134 F/cm³ | n/a | Interdigitated (27 cm, 8 μm) |
| CPE-K[91] | mS | n/a | 200 F/cm³ | n/a | Dual-Gate/Planar (27 cm, 8 μm) |
| CPE-K[43] | 120 mS | 14.7 F/cm·V·s | n/a | 0.1 cm²/(V s) | Interdigitated (3 cm, 8 μm) |
| n-type CPEs | | | | | |
| p(gNDI-T2)[94] | n/a | n/a | 190 F/cm³ | $1 \times 10^{-4}$ cm²/(V s) | Planar/Horizontal (100 μm, 10 μm) |
| p(gNDI-gT2)[94] | 0.022 mS | n/a | 397 F/cm³ | $1 \times 10^{-5}$ cm²/(V s) | Planar/Horizontal (100 μm, 10 μm) |
| p(C3-gNDI-gT2)[96] | 0.13 S/cm | 0.06 F/cm·V·s | 221 F/cm³ | $2.2 \times 10^{-4}$ cm²/(V s) | Planar/Horizontal (100 μm, 10 μm) |
| p(C3-gNDI-gT2)[96] | 0.34 S/cm | 0.13 F/cm·V·s | 72 F/cm³ | $9.2 \times 10^{-4}$ cm²/(V s) | Planar/Horizontal (100 μm, 10 μm) |
| p(C6-gNDI-gT2)[96] | 0.37 S/cm | 0.16 F/cm·V·s | 59 F/cm³ | $6.3 \times 10^{-4}$ cm²/(V s) | Planar/Horizontal (100 μm, 10 μm) |

[a]$g_m$ = transconductance; $\mu C^*$= product capacitance; $C^*$ = capacitance; $\mu$ carriers mobility; $n/a$ = not available; W = width; L = length.

## 2.5. Perspectives on COEs in Protein and Organelle Detection

As discussed in the above sections, the performance of COEs in protein detection is closely linked to their water solubility, hydrophobicity, electrostatic properties, and fluorogenic sensitivity when interacting with targets, see Table 1.[69] Opportunities exist to expand the photophysical properties into the far red or near-infrared (NIR) regions as instrumentation for these regions becomes more available. Note that COEs offer advantages for targeting proteins due to their smaller size and amphipathic tunable structures, which can be designed to target specific domains and pockets in proteins, such as the amyloid fibers presented here. These tunable structures also offer the possibility of expanding the types of targets, such as amyloid oligomers, or incorporating sensitive groups that can detect specific residues or post-translational modifications, such as phosphorylations or glycans. There are still opportunities to develop COEs that target other organelles, such as the nucleus, using hydrophilic cations, or lysosomes, using morpholine or dimethylamino substituents. To achieve this, comparative studies aimed at understanding how molecular structure influences cell membrane diffusion vs intercalation dependence need to be conducted. Several informative reviews on incorporating organelle-targeting functionalities are available, and we direct the reader to those resources.[70−73]

## 3. CPES IN ORGANIC ELECTROCHEMICAL TRANSISTORS SETTINGS

### 3.1. Fundamentals of Organic Electrochemical Transistors Settings

Organic mixed ionic-electronic conductors (OMIECs) is the conventional term used to refer to OSCs that can solvate ions and can be adapted to organic electrochemical transistors (OECTs) settings.[41,76] Note that all CPEs could be considered OMIECs, but not all OMIECs are CPEs. However, we will use OMIECs to also refer to CPEs in OECT settings during this section for consistency. OECTs interconvert (transduce) ionic signals into electrical signals, and they are the forefront candidates for this task due to their excellent and tunable ionic-electronic coupling/decoupling.[45,77−80] Transducing ionic signals into electrical signals and vice versa is of immediate bioelectronic interest, specifically for skin electronics and neural applications.[77,81]

The main figures of merit in this field are transconductance ($g_m$), product mobility/capacitance ($\mu C^*$), and volumetric capacitance ($C^*$). A higher $g_m$ value implies higher signal amplification, mainly depending on the materials' ionic-electronic coupling and electronic conduction.[82,83] At saturation conditions, one can construct a linear regression of the $g_m$ versus its channel geometry and biasing conditions, and the slope will give you $\mu C^*$.[9] The unit of $C^*$ is Farads (F), but $C^*$ in OECTs often is reported as volumetric capacitance (F/cm³). The $\mu C^*$ and $C^*$ are correlated with the effectiveness of storing electrical charges, which mainly depends on the efficiency of the OMIECs ion penetration, transport, and storage ability.[82−84] We emphasize that the device architecture, electro-ionic active-material thickness, and electrolyte identity of the OECTs play a significant role in the device's performance. Therefore, for an in-depth discussion of OMIECs in OECTs, you can also find recent reviews from McCulloch et al.,[77] Nielsen et al.,[78] Inal et al.,[84] and Rivnay.[41]

### 3.2. OECTs Based on P-type OMIECs

Conceptually, p-type OMIECs (or CPEs) exhibit quasi-stability upon oxidation, resulting in a weakly interacting electron−hole pair (polaron) with an optical transition within the NIR-IR window.[85,86] In p-type materials, their highest occupied molecular orbital (HOMO) levels are within the potential window of investigation. Therefore, it is possible to leave a hole in p-type OMIECs upon oxidation. To achieve p-type OMIECs, an electron-rich moiety must be included in the backbone.

Since 2013, PEDOT:PSS (Figure 6a) derivatives have been the main protagonists as active materials in OECT settings, with initial $g_m$ and $\mu C^*$ values approaching 5 mS and 50 F/cm·V·s, respectively.[9,80,82] One key contribution of this seminal OMIEC paper was highlighting how thickness might impact the OECT performance (see Figures 6b,c). Note that a (3-Glycidyloxypropyl)trimethoxysilane (GOPS) serves as an active layer cross-linker for making the PEDOT:PSS denser, reducing solubility in aqueous environments.[84,87] However, incorporating GOPS into the active layer of OECTs disrupts crystalline order and reduces free volume, compromising carrier mobility and volumetric capacity.[88,89] Amassian and co-workers published a breakthrough in the structural stabilization of PEDOT:PSS through electrostatic self-assembly (ESA) in 2024.[90] Via ESA, a solution of the active material is aged up to 4 days with Li-TFSI, resulting in enhanced cocrystal formation when deposited on the device. Optimal GOPS-free $g_m$ and $\mu C^*$
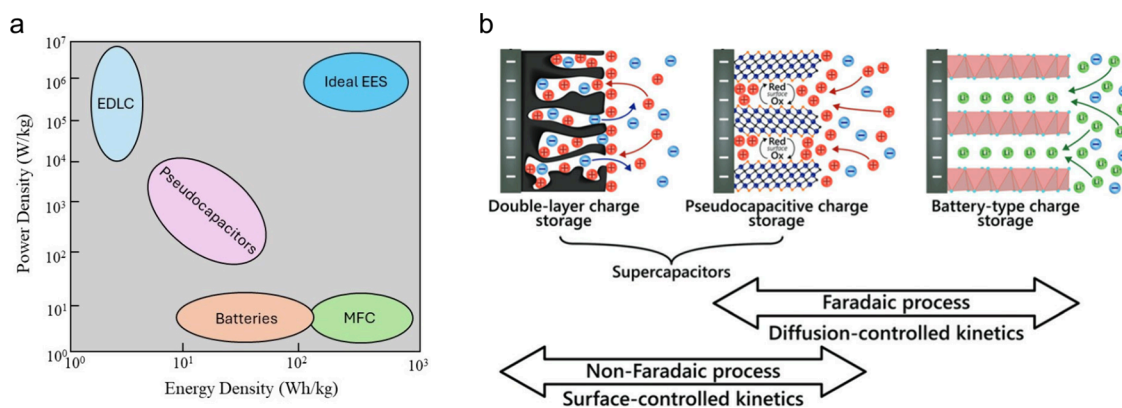
**Figure 7.** (a) The Ragone plot contextualizes power density versus energy density of different electrochemical energy storage devices such as EDLC, pseudocapacitors, batteries, and MFC. The ideal EES device must simultaneously possess high power and energy density. (b) Graphical depiction of the EDLC, pseudocapacitance, and battery charge-storage mechanism. Adapted with permission.[106] Copyright 2019, Wiley-VCH.

values of 31.4 mS and 752.5 F/cm·V·s were reported (Figure 6d and Table 2) for PEDOT:PSS using this approach, offering a simple yet effective sample processing techniques for GOPS-free OECT characterization.

Concerning the self-doped CPE-K (see Figure 6e), in 2020, Nguyen and co-workers reported an initial $g_m$ value approaching 4 mS and 70 mS in regular (Figure 6f) and interdigitated (Figure 6g) contacts, highlighting the importance of the device architecture in OECT performance.[42] That study also reported an optimal C* of 134 F/cm3, as determined by impedance spectroscopy. Note that this study used different concentrations of GOPS as cross-linkers, which significantly affected the device performance and conductivity of CPE-K. In 2023, Llanes et al. evaluated the impact of the side-chain engineering of CPE-K analogs on its OECT performance.[91] The alkyl chain length was tuned from 2 to 5 carbon atoms between the sulfonate unit and its π-conjugated backbone. For context, typical CPE-K has 4 carbons between the sulfonate unit and its π-conjugated backbone.[32,33,92] Results revealed a $g_m$ that was two times higher for the CPE-K derivatives with 3 to 5 carbons (~38.1 mS) between the sulfonate unit and their π-conjugated backbone compared to the CPE-K derivative with 2 carbons (18 mS), see Figure 6h.[91] Similar trends were observed when evaluating C*, as a value of 5.1 F/cm³ was reported for the CPE-K derivative with the shorter alkyl chain. In contrast, C* (~200 F/cm³) values two orders or magnitudes higher were obtained for the CPE-K derivatives with 3−5 carbons between the sulfonate unit and the π-conjugated backbone.

In 2024, Chae et al. investigated the impact of the molecular weight ($Mw$) of CPE-K on OECT performance. An optimal $g_m$ of 120 mS (Figure 6i) in interdigitated electrodes was reported for the CPE-K with intermediate $Mw$ values, attributed to superior carrier mobility (~0.1 cm²/(V s)).[43] A $\mu C$* (14.7 F/cm·V·s) that was 1 order of magnitude larger than that reported by Nguyen-Dang et al. in 2022 (see Figure 6i).[93] These findings highlight the complex interplay of device architecture, OMIECs identity and composition, side-chain engineering, and $Mw$ for optimal OECT performance.

### 3.3. OECTs Based on N-type OMIECs

Conceptually, n-type OMIECs (or CPEs) refer to systems that show quasi-stability upon reduction, resulting in a weakly interacting electron−hole pair (polaron) with an optical transition within the NIR-IR window.[86,94] Another way to

conceptualize n-type OMIECs is that their lowest unoccupied molecular orbital (LUMO) levels are within the potential window of investigation. Therefore, inserting an electron in n-type OMIECs upon reduction is possible. To achieve n-type CPEs, an electron-deficient moiety must be included in the polymer's backbone.

In 2016, Giovannitti et al. reported n-type OMIECs using NDI derivatives, namely p(gNDI-T2) and p(gNDI-gT2), see Figure 6j.[94] The main difference between the p(gNDI-T2) and p(gNDI-gT2) OMIECs is that the former has hydrogen atoms in their thiophene linker, while the latter replaces the hydrogen atoms with extra pegylated side chains, often translating to enhanced ionic conductivity.[95] As a result, a C* that was two times higher was obtained for the p(gNDI-gT2), see Table 2.[94] For p(gNDI-gT2), a detectable $g_m$ of 0.022 mS was reported, see Figure 6k. In contrast, the $\mu$ for p(gNDI-T2) could not be resolved, as the resulting currents were below the measurement sensitivity for the device. This study highlighted the importance of a pegylated side chain to promote ion transport and enable aqueous operation, and provided proof of concept for OMIECs dual operation in n-type and p-type configurations (ambipolar).

In 2021, a subsequent study by Maria et al. probed the effect of alkyl spacers between the NDI and the ethyl acetate functional group on their OECT performances, namely p(gNDI-gT2), p(C3-gNDI-gT2), and p(C6-gNDI-gT2).[96] In all cases, the thiophene linkers were pegylated and are derivatives from the OMIEC in Figure 6j. A minimal impact on the oxidation potential was found between p(gNDI-gT2) and p(C3-gNDI-gT2), but a reduction onset of −0.1 V versus Ag/AgCl was found for the p(C6-gNDI-gT2), see Figure 6l, which was explained by a lower degree of swelling and potentially lower ionic mobility.[96,97] Although the alkyl incorporation lowered C*, results revealed a higher $g_m$ and $\mu C$* for the investigated n-type OMIECs upon alkyl incorporation. Specifically, a $g_m$ of 0.17 S/cm, 0.34 S/cm, and 0.37 S/cm for p(gNDI-gT2), p(C3-gNDI-gT2), and p(C6-gNDI-gT2), respectively, were obtained when normalized by film thickness, see Figure 6m. In the case of $\mu C$*, 0.06 F/cm·V·s, 0.13 F/cm·V·s, and 0.16 F/cm·V·s were reported for p(gNDI-gT2), p(C3-gNDI-gT2), and p(C6-gNDI-gT2), respectively, see Table 2. These results were explained in the context of alkyl spacers limiting detrimental swelling of the investigated OMIECs in aqueous media while enabling reversible redox reactions at low potentials.[96]
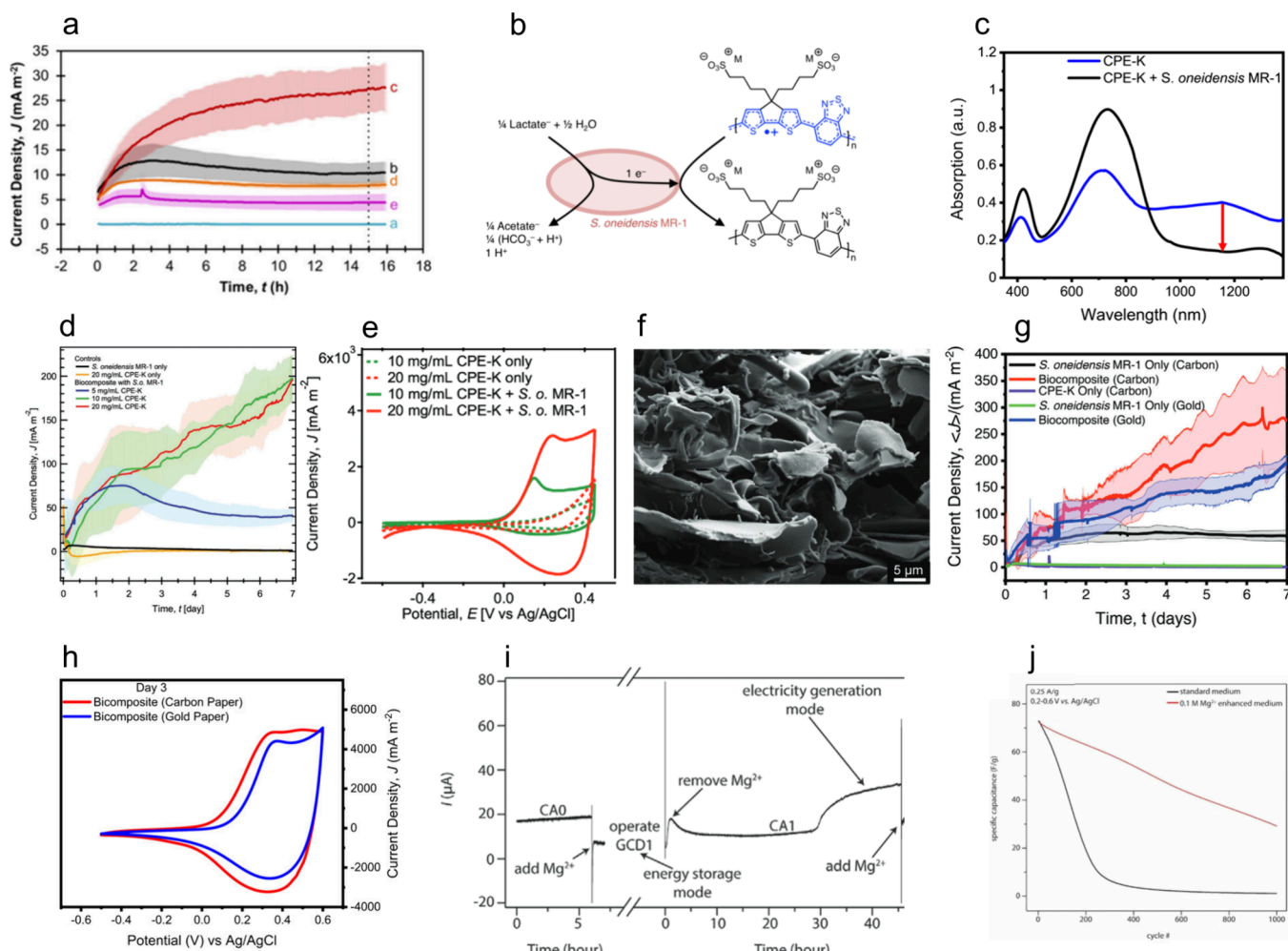
**Figure 8.** (a) Biocurrent production from *S. oneidensis* MR-1 amplified by CPE-K, (b) the proposed electron transfer mechanism between *S. oneidensis* MR-1 and CPE-K, (c) and the electron transfer impact on the polaron of CPE-K. Adapted with permission.[117] Copyright 2017, Wiley-VCH. (d) Biocurrent generation of the CPE-K/*S. oneidensis* MR-1 biocomposite, (e) their respective voltammograms showing pseudocapacitive characteristics, and (f) SEM images of the 20 mg/mL biocomposite. Adapted with permission.[113] Copyright 2017, Wiley-VCH. (g) Biocurrent generation comparison of 20 mg/mL biocomposite on porous carbon paper and gold electrodes and (h) their voltammograms after 3 days of operation showing enhanced pseudocapacitive characteristics in porous carbon paper. Adapted with permission.[114] Copyright 2022, Wiley-VCH. (i) Biocurrent generation and (j) pseudocapacitive cycling stability of 20 mg/mL biocomposite on gold working electrodes, which can switch operation from biocurrent production to enhanced pseudocapacitive behavior by adding $Mg^{2+}$. Adapted with permission.[120] Copyright 2021, Wiley-VCH.

## 3.4. Perspectives on CPEs in OECT Settings

The OECT performance depends on the complex interplay between device architecture, OMIEC identity and composition, side-chain engineering, and *Mw*. It is worth noting that the design and synthesis of new OMIECs with low driving voltage, low power consumption, and enhanced biocompatibility are needed to optimize their utility. However, the current thinking is that OMIEC processing must be prioritized to achieve crystalline domains with high electron−ion coupling, carrier mobility, ionic conductivity, and high swelling stability to yield enhanced OECT performance. For example, the cross-linker free solution aging approach for promoting enhanced crystalline domains through electrostatic self-assembly (ESA), as reported by Amassian and co-workers, demonstrates how subtle yet insightful material management can lead to superior OECT performance.[90] In addition, new self-doped CPEs with tuned threshold voltage are needed.[98−100]

## 4. CPES IN ELECTROCHEMICAL ENERGY STORAGE SETTINGS

### 4.1. Fundamentals of EES

Electrochemical energy storage (EES) is an umbrella term encompassing electron and ion transfer mechanisms responsible for converting chemical energy into electrical energy (charges).[101,102] Electrochemical double-layer capacitance (EDLC), pseudocapacitance, batteries, and fuel cells (including microbial - MFC) better describe the four main devices or mechanisms of EES. The Ragone plot (Figure 7a) compares their performance in terms of power density (W/kg) versus energy density (Wh/kg), which is a normalized way to express their performance for better comparison.[103] Note that the ideal EES device will simultaneously exhibit high power and energy density. To achieve this goal, a fundamental understanding of the mechanisms for storing and releasing electrical charges on demand is needed.

The EDLC mechanism is associated with supercapacitors, which store charges via reversible ion-dependent electrostatic interactions (nonfaradaic).[104,105] Batteries store charges via reversible redox processes (faradaic).[106] Pseudocapacitors employ reversible redox chemistry coupled with a concomitant ion-dependent electrostatic insertion.[104,106,107] A depiction of these mechanisms can be observed in Figure 7b. Regarding MFC, microorganisms oxidize chemical feedstock, generating electrons that can be harvested (biocurrent), and are often reported in terms of current density.[108,109] We emphasize that the charge storage mechanism determines the device's performance and stability. Therefore, for an in-depth discussion of the mechanism governing these EES technologies, you can find recent reviews from Mathis et al.,[106] Fleischmann et al.,[104] Logan et al.,[108,109] and McCuskey et al.[110]

It is worth noting that MFCs are often discussed in terms of benchmarking current density (A/m$^2$) values.[111] Batteries possess high energy density, meaning they can hold a sizable amount of electrical charges but release them slowly.[112] Power density refers to the number of charges that can be delivered at a given time and is normalized by the electroactive material weight (W/kg) or by the current collector area (W/cm$^2$) or volume (W/cm$^3$). However, the performance of capacitors and pseudocapacitors is more often reported in terms of capacitance ($C^*$), and within this context, $C^*$ describes the geometrical effectiveness of storing electrical charges.[82−84]

CPEs exhibit a charge-storing mechanism that more closely resembles pseudocapacitive behavior. Pseudocapacitors' cycling stability or life cycle, which indicates how many times the material can be charged and discharged while maintaining high performance, is a figure of merit. Note that specific current (A/g) and current density (A/cm$^2$) refer to the charge/discharging rate of operation. The former refers to the applied current per mass loading, while the latter refers to the applied current per current collector area. Both terminologies benchmark how fast a material can be charged/discharged. The ideal pseudocapacitor should exhibit high cycling stability at the highest possible charge/discharging rate of operation.

## 4.2. Interfacing CPEs in Microbial Fuel Cell Settings

Metabolic pathways in bacteria can be utilized to our advantage in materials and technology development.[113−115] This realm of technology is known as bioelectrochemical systems (BES), and it transforms chemical feedstocks into value-added products. However, efficient microbial colonization and electronic communication with electrode surfaces are required to maximize the performance of a given BES.[116] In 2017, Kirchhofer et al. explored the anaerobic respiration of an electrogenic bacteria, *Shewanella oneidensis* MR-1 (*S. oneidensis* MR-1), on CPEs with different molecular structures.[117] Direct electron transfer (DET) and mediated electron transfer (MET) are the primary exoelectronic mechanisms of this microorganism for biocurrent production through lactate oxidation.[118] The former directly interacts with the electrode, typically involving transmembrane redox-active protein, as it has also been observed when COEs are used for electron harvesting.[119] The latter relies on diffusible redox mediators like flavins to shuttle electrons across the insulating cell membrane. Chronoamperometry (CA) measurements were carried out at a poised potential of 0.3 V vs Ag/AgCl to account for the oxidation state of the CPEs and the DET and MET electrochemistry of *S. oneidensis* MR-1.[117] Interestingly,

CPE-K was the only CPE (c, in Figure 8a) that increased biocurrent production over the control experiments (b, in Figure 8a), see Table 3. For example, the reactor with CPE-K

**Table 3. Summary of the Biocurrent Performances When Interfacing CPE-K with *S. oneidensis* MR-1 for Biocurrent Amplification[a]**

| CPE | Incorporation | Control Biocurrent | Experimental Biocurrent | Electrode/Current Collector Type |
|---|---|---|---|---|
| CPE-K[117] | Additive (10 μM) | 10.4 mA/m$^2$ | 27.5 mA/m$^2$ | Carbon Felt |
| CPE-K[113] | Hydrogel | 1.6 mA/m$^2$ | 198 mA/m$^2$ | Gold Electrode |
| CPE-K[114] | Hydrogel | 49 mA/m$^2$ | 279 mA/m$^2$ | Carbon Paper |
| CPE-K[120] | Hydrogel | *n/a* | 150 mA/m$^2$ | Gold Electrode |

[a]Note that the experiments here have different designs, so the length of chronoamperometric characterization for biocurrent density determination might vary.

achieved a steady current density of 27.5 mA/m$^2$ after 16 h of operation, while the current density for the control system was 10.3 mA/m$^2$. Further experimentation revealed that CPE-K is reduced upon receiving electrons from *S. oneidensis* MR-1 (Figure 8b) after lactate oxidation.[113] This reduction ultimately enhances electron transfer efficiency from the bacteria to the electrode with CPE-K as a mediator, as evidenced by the disappearance of the polaronic optical transition band and the increase of the neutral species transition band (Figure 8c).

In 2020, McCuskey et al. reported a CPE-K/*S. oneidensis* MR-1 biocomposite capable of extracting a biocurrent of 198 mA/m$^2$ (Figure 8d), also showing pseudocapacitive characteristics (Figure 8e). The improved performance was attributed to the formation of a 3D conductive and pseudocapacitive network (see Figure 8f). From the Kirchhofer and McCuskey experiments, note that the biocurrent generation from S. *oneidensis* MR-1 in control experiments was highly dependent on the nature of the working electrodes, with 10.3 mA/m$^2$ (Figure 8a) and 1.6 mA/m$^2$ (Figure 8d) reported for carbon and gold electrodes, respectively. Therefore, Vázquez et al. characterized the same biocomposite (CPE-K/*S. oneidensis* MR-1) in carbon electrodes, following the same approach from McCuskey et al. Results revealed a biocurrent amplification of ~1.5-fold higher for the biocomposite in carbon electrodes (279 mA/m$^2$) than in gold electrodes (198 mA/m$^2$) after 7 days of operation, see Figure 8g.[114] CV traces revealed that the biocomposite assembled more quickly in the porous structure of the carbon paper than in the flat gold electrodes, as suggested by the pseudocapacitive traces, see Figure 8h. For example, daily CV measurements revealed that the pseudocapacitive conductive networks were stable after 3 days of operation in carbon paper, while it took 5 days to stabilize in flat-gold electrodes. This earlier pseudocapacitive stabilization could explain the biocurrent amplification, as harvesting electrons via long-range energy transport occurs in the earlier days of operation.[114]

In 2021, Su et al. demonstrated that the **CPE-K/*S. oneidensis* MR-1** biocomposite can switch functions between biocurrent generation and pseudocapacitor in response to external stimuli, see Figure 8i. The key difference between this study and the previous ones was adding a defined amount of MgSO$_4$ (0.1 M)
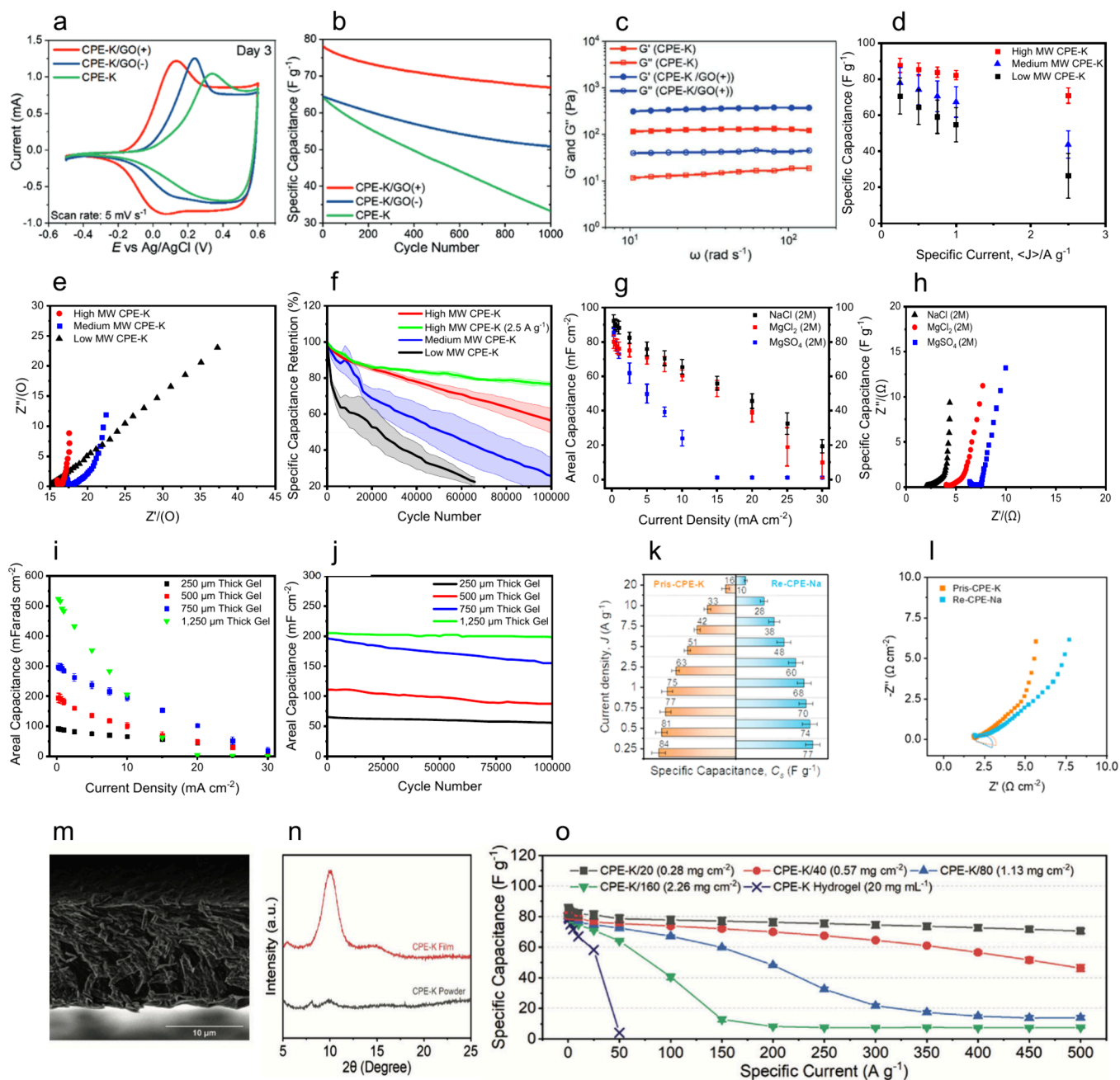
**Figure 9.** (a) Influence of 2D graphene-based electrolytes in the pseudocapacitive traces, (b) cycling stability, and (c) gel-like properties of CPE-K hydrogels. Adapted with permission.[125] Copyright 2022, Wiley-VCH. The influence of the molecular weight of CPE-K hydrogels on (d) their specific capacitance, (e) their ideal capacitive behavior, and (f) their cycling stability in $Mg^{2+}$ enriched solutions. Adapted with permission.[126] Copyright 2022, RSC. The influence of the electrolyte's identity on the (g) specific capacitance and (h) ideal capacitive behavior of CPE-K hydrogels. Thickness dependence (i) areal capacity and (j) cycling stability at 10 mF/cm² of CPE-K hydrogels in 2 M NaCl electrolyte solution. Adapted with permission.[33] Copyright 2023, RSC. (k) The specific capacitance and (l) the ideal capacitive behavior comparison between pristine and recycled CPE-K hydrogels. Adapted with permission.[92] 2023, ACS. (m) SEM images of CPE-K thin film after slow evaporation casting and (n) its X-ray diffraction pattern comparison with powder CPE-K. (o) The specific capacitance of CPE-K thin films of different mass-loadings at different specific currents. Adapted with permission.[32] Copyright 2024, Wiley-VCH.

to the reservoir at different time points. Results revealed that adding $Mg^{2+}$ immediately **reduced** the biocurrent production (Figure 8i) while enhancing its pseudocapacitive performance's cycling stability, see Figure 8j.[120] Interestingly, biocurrent generation was **restored** after replacing the $Mg^{2+}$-enriched solution with fresh media, as the bacteria **began** to grow again. In all cases, the specific capacitance reported in this study was 73 F/g when cycled at a specific current of 0.25 A/g. However,

the **CPE-K**/*S. oneidensis* **MR-1** biocomposite in the $Mg^{2+}$-enriched electrolyte retained 40% of its initial capacitance after 1000 cycles, while the capacitance of the biocomposite without the $Mg^{2+}$ in the medium dropped to 0 after ∼250 cycles, see Figure 8j. This improvement was explained by the bidentate nature of $Mg^{2+}$, allowing for intermolecular cross-linking of CPE-K.[120−122] These seminal findings **highlighted** the importance of interfacing CPEs in different EES settings,

**Table 4. Summary of the Optimal Biocurrent Performances in Three and Two Electrode Settings[a]**

| CPE-K Incorporation | Electrolyte | Capacitance | Life Cycle |
|---|---|---|---|
| Biocomposite[120] (gold electrode) | SM | 75 F/g at 0.25 A/g | 0 F/g after 250 cycles at 0.25 A/g |
| Biocomposite[120] (gold electrode) | Mg$^{2+}$ Enriched SM | 75 F/g at 0.25 A/g | 30 F/g after 1000 cycles at 0.25 A/g |
| Biocomposite[114] (gold electrode) | SM | 70 F/g at 0.25 A/g | 0 F/g after 250 cycles at 0.25 A/g |
| Biocomposite[114] (carbon paper) | SM | 70 F/g at 0.25 A/g | 25 F/g after 1000 cycles at 0.25 A/g |
| Hydrogel[125] (gold electrode) | GO$^+$ Enriched SM | 78 F/g at 0.25 A/g | 68 F/g after 1000 cycles at 0.25 A/g |
| Hydrogel High *Mw*[126] (gold electrode) | Mg$^{2+}$ Enriched SM | 88 F/g at 0.25 A/g<br>70 F/g at 2.5 A/g | 54 F/g after 100 K cycles at 2.5 A/g |
| Hydrogel Medium *Mw*[126] (gold electrode) | Mg$^{2+}$ Enriched SM | 78 F/g at 0.25 A/g<br>67 F/g at 1 A/g | 15 F/g after 100 K cycles at 1 A/g |
| Hydrogel Low *Mw*[126] (gold electrode) | Mg$^{2+}$ Enriched SM | 71 F/g at 0.25 A/g<br>54 F/g at 1 A/g | 0 F/g after 60 K cycles at 1 A/g |
| Hydrogel 250 $\mu$m[33] (gold electrode) | 2 M MgSO$_4$ | 85 mF/cm$^2$ at 0.25 mA/cm$^2$<br>22 mF/cm$^2$ at 10 mA/cm$^2$ | 21 mF/cm$^2$ after 10 K cycles at 10 mA/cm$^2$ |
| Hydrogel 250 $\mu$m[33] (gold electrode) | 2 M MgCl$_2$ | 81 mF/cm$^2$ at 0.25 mA/cm$^2$<br>60 mF/cm$^2$ at 10 mA/cm$^2$ | 57.6 mF/cm$^2$ after 10 K cycles at 10 mA/cm$^2$ |
| Hydrogel 250 $\mu$m[33] (gold electrode) | 2 M NaCl | 92 mF/cm$^2$ at 0.25 mA/cm$^2$<br>66 mF/cm$^2$ at 10 mA/cm$^2$ | 56.7 mF/cm$^2$ after 100 K cycles at 10 mA/cm$^2$ |
| Hydrogel 500 $\mu$m[33] (gold electrode) | 2 M NaCl | 194 mF/cm$^2$ at 0.25 mA/cm$^2$<br>103 mF/cm$^2$ at 10 mA/cm$^2$ | 88 mF/cm$^2$ after 100 K cycles at 10 mA/cm$^2$ |
| Hydrogel 750 $\mu$m[33] (gold electrode) | 2 M NaCl | 298 mF/cm$^2$ at 0.25 mA/cm$^2$<br>195 mF/cm$^2$ at 10 mA/cm$^2$ | 166 mF/cm$^2$ after 100 K cycles at 10 mA/cm$^2$ |
| Hydrogel 1,250 $\mu$m[33] (gold electrode) | 2 M NaCl | 523 mF/cm$^2$ at 0.25 mA/cm$^2$<br>205 mF/cm$^2$ at 10 mA/cm$^2$ | 180 mF/cm$^2$ after 100 K cycles at 10 mA/cm$^2$ |
| Thin-Film (0.28 mg/cm$^2$)[32] (Glassy Carbon) | 2 M KCl | 82 F/g at 0.25 A/g<br>82 F/g at 35 A/g<br>78 F/g at 100 A/g<br>71 F/g at 500 A/g | 80 F/g after 100 K cycles at 35 A/g |
| Thin-Film (0.57 mg/cm$^2$)[32] (Glassy Carbon) | 2 M KCl | 82 F/g at 0.25 A/g<br>74 F/g at 100 A/g<br>46 F/g at 500 A/g | *n/a* |
| Thin-Film (1.13 mg/cm$^2$)[32] (Glassy Carbon) | 2 M KCl | 82 F/g at 0.25 A/g<br>67 F/g at 100 A/g | *n/a* |
| Thin-Film (2.26 mg/cm$^2$)[32] (Glassy Carbon) | 2 M KCl | 82 F/g at 0.25 A/g<br>41 F/g at 100 A/g | *n/a* |

[a]The thickness of all biocomposite or hydrogels was 250 $\mu$m unless indicated otherwise. SM refers to the standard medium used for biocurrent generation, which was used when the pseudocapacitive properties of CPE-K were discovered by McCuskey et al.

opening an area of investigation for using CPE-K for pseudocapacitive applications, which will be discussed in the next section.

### 4.3. Perspectives on Interfacing CPEs in Microbial Fuel Cell Settings

The metabolic pathways of electrogenic bacteria can be coupled with materials technology to amplify biocurrent generation.[108,113] It was demonstrated that CPE-K formed a pseudocapacitive 3D conductive hydrogel where the bacteria can reside so that long-range electron harvesting can occur. This biocurrent amplification, in addition, is linked to healthy biofilm growth due to biocompatibility with carbon.[110,113,123,124] The current thinking is that CPEs should be introduced into two-electrode MFC devices. However, one limitation of introducing available CPEs into MFCs is their unsuitable redox potential relative to the oxygen reduction reaction (ORR), which typically closes the electrochemical circuit in MFCs using air cathodes.[108,124] At pH 7, the theoretical potential for ORR is +0.195 V vs Ag/AgCl, which limits the operating voltage of the MFC when paired with CPE-K. Therefore, optimizing the physico-electrochemical properties of CPEs hydrogels with complementary redox potential so that the MFC's operating voltage is widened is

necessary. In addition, bacterial engineering is needed to optimize their electrogenicity and possibly tune their redox potential for direct and mediated electron transfer, which is the mechanism by which electrogenic bacteria give electrons.[118]

### 4.4. CPEs for Pseudocapacitive Applications

Quek et al. explored the influence of adding 2D electrolytes, namely cationic (GO$^+$) or anionic (GO$^-$) graphene oxide, on the pseudocapacitive performance of CPE-K in abiotic conditions.[125] A similar electrolyte solution to that from Su et al. was used for this characterization, but graphene oxides were added instead of Mg$^{2+}$. Results revealed that adding GO$^+$ increases the specific capacitance of CPE-K from 65 F/g in neat conditions to 78 F/g when characterized with a specific current of 0.25 A/g, see Figure 9a and Table 4. Although the GO$^-$ did not increase the specific capacitance of CPE-K relative to that for the control experiments, both investigated graphene oxides increased the cycling stabilities of CPE-K (Figure 9b). Rheological measurements revealed that the GO$^+$ increased the gel-like elastic solid properties of the CPE-K, see Figure 9c. These results highlighted that electrolyte selection not only influences the electrochemical properties of CPE-K but also could change its mechanical properties. In addition, this study further confirmed that, under the conditions tested,

CPE-K becomes a conductive hydrogel with pseudocapacitive properties.

In 2022, Vázquez et al. demonstrated a positive correlation between the $Mw$ and the pseudocapacitive performance of CPE-K hydrogels. For example, the CPE-Ks with $Mw$ of 18 794 g/mol, 23 038 g/mol, and 31 960 g/mol had a specific capacitance of 71 F/g, 78 F/g, and 88 F/g, respectively, see Figure 9d and Table 4.[126] The verticalization at lower frequencies of the Nyquist revealed more facile ion diffusion within the conductive network of the high $Mw$ CPE-K hydrogel, see Figure 9e.[107] The high $Mw$ CPE-K retained over 50% of its specific capacitance at all conditions tested, including when tested at 1 A/g and 2.5 A/g, see Figure 9f. Rheological measurements revealed a positive correlation between the $Mw$ of CPE-K and its gel-like elastic solid response, indicating that increasing the $Mw$ of CPE-K results in hydrogels with greater mechanical strength.[127,128] Altogether, these results are a significant advancement, as a 100-fold increase in cycling stability over previously reported CPE-K hydrogels was obtained.[40]

A follow-up study in 2023 by Vázquez et al. investigated the influence of electrolyte identity and thickness on the pseudocapacitive properties of CPE-K hydrogels, focusing on 2 M concentrations of $MgSO_4$, $MgCl_2$, and NaCl.[33] The studies were carried out in terms of areal capacitance and current density, as the goals were to determine whether one can store more charges in CPE-K hydrogels per footprint area of the current collector. As observed in Figure 9g, the investigated electrolytes have minimal impact on the areal capacitance ($\sim$90 mF/cm$^2$) of the hydrogels at low current densities. Still, their areal capacitance is compromised when cycled at higher current densities. For instance, the areal capacitance of the CPE-K hydrogels in 2 M $MgSO_4$ electrolytes goes to 0 at 15 mA/cm$^2$. In contrast, a sizable areal capacitance close to 60 mF/cm$^2$ was found at 15 mA/cm$^2$ for the CPE-K hydrogels in 2 M $MgCl_2$ and NaCl electrolytes. The Nyquist plot analysis revealed that CPE-K hydrogels in NaCl electrolytes have a lower equivalent series resistance and a more ideal pseudocapacitive behavior than in other electrolytes tested, as evidenced by the vertical line in the Warburg region, see Figure 9h.

Thickness-controlled experiments in NaCl electrolytes were conducted, and a positive correlation between the hydrogel thickness and its areal capacitance was found, see Figure 9i. For example, the areal capacitance for the 250 $\mu$m, 500 $\mu$m, 750 $\mu$m, and 1,250 $\mu$m thick hydrogels was 92 mF/cm$^2$, 194 mF/cm$^2$, 298 mF/cm$^2$, and 523 mF/cm$^2$, respectively, at a current density of 0.25 mA/cm$^2$. However, increasing the gel thickness compromises their capacitances at higher current densities, Figure 9i. The current thinking is that the redox-active sites of CPE-K are less accessible to anions for ionic-electronic at higher charge/discharge rates upon increasing the hydrogel thickness.[33] However, the thickness seems to have minimal impact on the cycling stability of the gels, as areal capacitance retention >85% was obtained after 100,000 cycles were carried out at 10 mA/cm$^2$, see Figure 9j and Table 4. This study accentuated the use of CPE-K for high mass/electrode loadings to potentially enhance the energy density of pseudocapacitive electrodes while maintaining the same current collector footprint.

In 2024, Jiang et al. introduced CPE-K hydrogels as recyclable, electrochemically stable, and eco-friendly pseudocapacitive materials. Removing the CPE-K hydrogel from the electrochemical cell after initial assessment for recasting and electrochemical reassessment was performed. Note that the recycling workup has no significant detrimental impact on the electrochemical performance, see Figure 9k.[92] For example, pristine CPE-K hydrogels showed an initial specific capacitance of 33 F/g when cycled at 10 A/g, decreasing to 24 F/g after 100,000 cycles. After recycling and recasting, the same CPE-K formed a hydrogel with a specific capacitance of 26 F/g when cycled at 10 A/g, decreasing to 21 F/g after 100,000 cycles. Electrochemical impedance spectroscopy revealed that the recasted CPE-K hydrogel exhibited reduced ideal capacitive behavior than pristine CPE-K materials, see Figure 9l. Interestingly, no discernible difference was obtained when structurally characterizing the pristine and recasted CPE-K hydrogels. However, one difference noted comes from GPC analysis, where recycled CPE-K had a number-average molecular weight of 100 000 g/mol, while that for the pristine was 113 000 g/mol, possibly influencing the mechanical properties of the hydrogels.

That same year, Bazan and co-workers demonstrated that it is possible to create thin film pseudocapacitive electrodes for characterization in aqueous environments from previously water-soluble CPE-K hydrogels, see Figure 9m. The key technical approach for creating the thin-film electrode of CPE-K is by slow evaporation after hydrogel drop casting so that spontaneous crystalline domains can be formed, as revealed by X-ray diffraction, see Figure 9n.[32] Note that the CPE-K film exhibited a strong peak at 10.1°, indicative of ordered domains not observed in the powder form. All CPE-K electrodes showed similar specific capacitance to that in the hydrogel form ($\sim$90 F/g) when cycled at low specific currents, regardless of the mass loading, see Figure 9o. However, CPE-K electrodes with a mass loading of 0.28 mg/cm$^2$ showed unprecedented specific capacitance retention (71 F/g) when cycled at 500 A/g, see Table 4. When the mass loading of the CPE-K was 1.13 mg/cm$^2$, the capacitance retention was $\sim$67 F/g when cycled at 100 A/g, a figure of merit for pseudocapacitive materials when it comes to charging/discharging rates. Excellent cycling stability was obtained in all cases regardless of the CPE-K mass-loading.

## 4.5. Perspectives on CPEs for Pseudocapacitive Applications

As discussed in previous sections, pseudocapacitive performance depends on the complex interplay between electrolyte selection, ionic conductivity within the electroactive material, side-chain engineering, and optimizing $Mw$. A key finding correlated enhanced mechanical properties of CPE-K hydrogels with optimal pseudocapacitive performance. However, the slow evaporation of CPE-K hydrogels after drop casting, as reported by Yip et al., was responsible for yielding thin-film electrodes with crystalline domains.[32] As a result, it was possible to access unprecedented pseudocapacitive performances that are figures of merit in the field. The current thinking is that material processing to achieve crystalline domains with high electron−ion coupling, carrier mobility, ionic conductivity and stability will yield superior pseudocapacitive performance. This becomes more apparent when we contextualize the pseudocapacitive discussion with the OECTs discussion. As detailed in the OECTs section, an OMIECs/electrolyte aging approach promoted electrostatic self-assembly (ESA). These two examples demonstrate how subtle, yet insightful material management can produce superior OECT performance.[90]
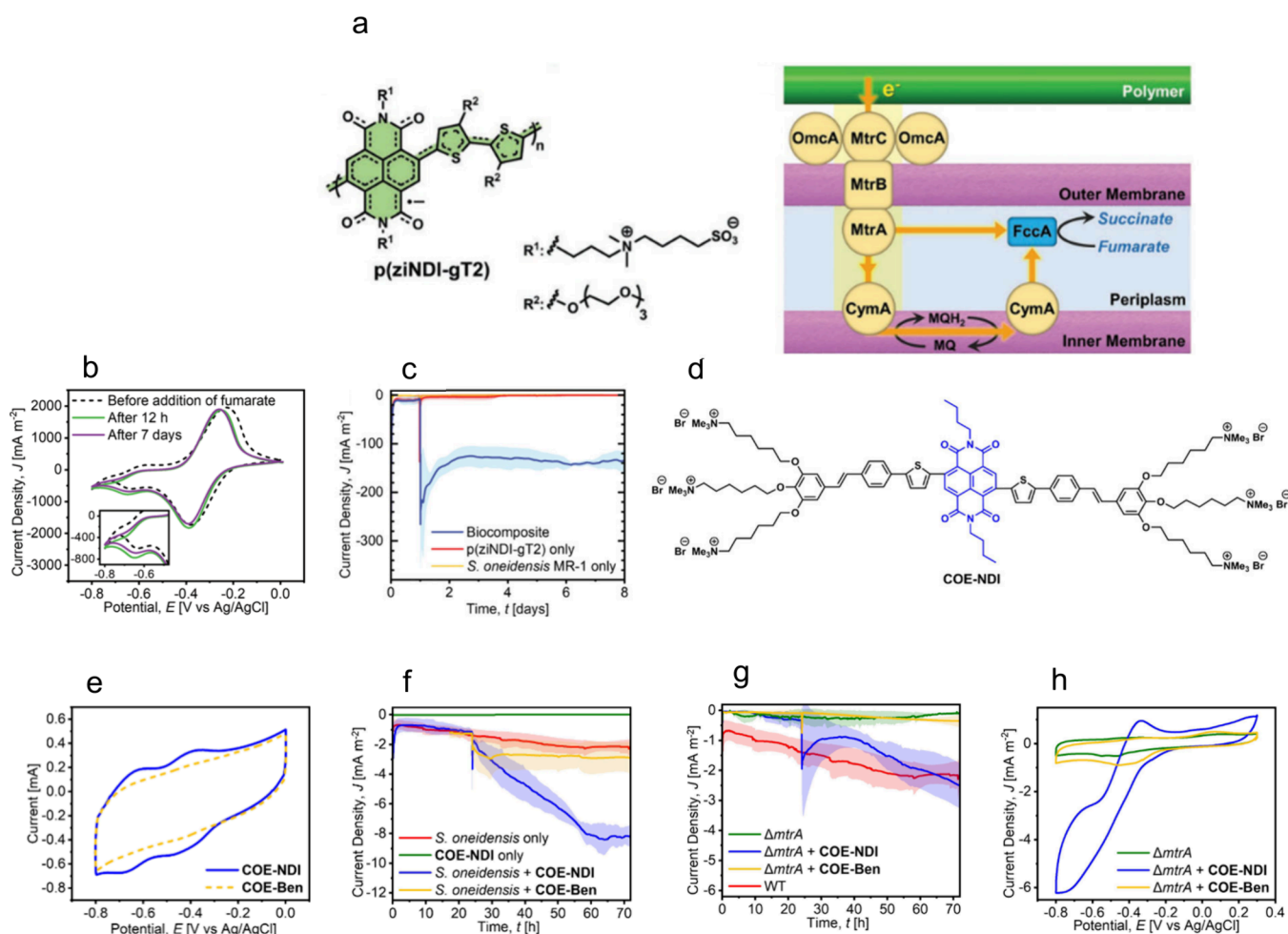
**Figure 10.** (a) The molecular structure of p(ziNDI-gT2) and the proposed model for the extracellular electron uptake by *S. oneidensis* MR-1 through its MtrCAB respiratory pathway. (b) Voltammograms of the p(ziNDI-gT2) and (c) the biocurrent amplification of the p(ziNDI-gT2)/*S. oneidensis* MR-1 biocomposite. Adapted with permission.[133] Copyright 2022, Wiley-VCH. (d) Molecular structure of COE-NDI, (e) its voltammogram traces, and (f) its chronoamperometry measurements showing biocurrent amplification for the COE-NDI/*S. oneidensis* MR-1 complex. (g) Biocurrent amplification and (h) their respective voltammogram traces of the COE-NDI/*S. oneidensis* MR-1 mutant complex. Adapted with permission.[28] Copyright 2023, Wiley-VCH.

Interdigitated electrodes improved the OECT performance in OMIECs. Consequently, architectural design that optimizes current collection structures might also be needed for optimal pseudocapacitive performance. In parallel with these efforts, designing and synthesizing new CPEs with a broader operating potential that matches that of aqueous environments is desirable. In addition, systematic studies are needed to understand self-doping formation and how it affects hole, charge, and ion transport.[23]

## 5. INTERFACING CPES AND COES IN BIOELECTROSYNTHETIC SETTINGS

### 5.1. Fundamentals of Bioelectrosynthetic Settings

It is possible to inject electrons into the metabolic pathway of electrogenic bacteria to convert chemical feedstocks into value-added products, an iteration of bioelectrochemical systems (BES).[129,130] Another way of thinking about BES for bioelectrosythesis is as a biocatalyst, where enzymes or cells replace traditional catalysts to access unattainable chemical transformations.[131] However, in bioelectrosynthesis, using electricity to drive these biocatalytic reactions is of interest instead of using traditional biological pathways. One of the

main technical limitations of bioelectrosynthesis is the poor biotic/abiotic interface, which limits enhanced electron transfer from the electrode to the biocatalytic entity.

### 5.2. Interfacing CPEs in Bioelectrosynthetic Settings

In 2022, Quek et al. envisioned a 3D conductive network where *S. oneidensis* MR-1 resides in an n-type CPE hydrogel so long-range electron transfer from the electrode to the BES could occur. The synthesized n-type CPE was p(ziNDI-gT2), which possesses a similar NDI subunit as the materials discussed in the n-type OECT section, as shown in Figure 10a. For efficient electron transfer to occur, p(ziNDI-gT2) must have a LUMO energy level more negative than that for *S. oneidensis* MR-1's outer membrane-spanning MtrCAB protein complex, which is known to participate in the fumarate to succinate reduction process.[132] The redox activity of the LUMO energy levels of p(ziNDI-gT2) was confirmed via cyclic voltammetry, see Figure 10b. For context, the MtrCAB protein complex is known to have a redox response within −0.20 V to −0.65 V vs Ag/AgCl, and so is p(ziNDI-gT2).[133] A 20 mg/mL of p(ziNDI-gT2)/*S. oneidensis* MR-1 biocomposite was prepared, following the experimental approach discussed in the MFC section for the CPE-K/*S. oneidensis* MR-

1biocomposite. The key chronoamperometric difference in these experiments over electron harvesting was setting the potential to −0.56 V vs Ag/AgCl during operation.

Results revealed a current amplification of ∼674 times for the biocomposite compared to the control experiments with the same initial number of cells (see Figure 10c), presumably enabling continuous succinate synthesis from fumarate. Integration of the biocurrent amplification showed that 99% of the electrons injected into *S. oneidensis* MR-1 through the biocomposite were part of the reduction of fumarate to succinate, as indicated by the HPLC evaluation for succinate generation. To provide evidence that p(ziNDI-gT2) injects electrons into *S. oneidensis* MR-1 cells via the MtrCAB respiratory pathway, mutant strains lacking specific MtrCAB construct components were employed. Results revealed minimal biocurrent amplification for the mutants compared to the wild type, highlighting the importance of the MtrCAB protein complex of *S. oneidensis* MR-1 for important electrogenic processes. In addition, these results demonstrated that incorporating 3D conductive networks with n-type CPEs is an effective method to amplify current injection in bioelectrosynthesis.

### 5.3. Interfacing COEs in Bioelectrosynthetic Settings

In 2023, Quek et al. reported an n-type membrane-intercalating COE, COE-NDI (see Figure 10d), for fumarate to succinate bioelectrosynthetic amplification using similar principles to those for the p(ziNDI-gT2)/*S. oneidensis* MR-1 biocomposite.[28] Cyclic voltammetry measurements (Figure 10e) confirmed the LUMO energy levels of COE-NDI were suitable for satisfying the electrochemistry associated with the MtrCAB protein complex. Chronoamperometric measurements revealed a 3-fold biocurrent amplification for the COE-NDI/*S. oneidensis* MR-1 complex over the control experiments, including when other COEs with unsuitable LUMO levels were used, see Figure 10f. A mutant strain of the MtrCAB construct with interrupted transmembrane protein domains was employed in this study as well. Results revealed that incorporating the COE-NDI into the mutant resulted in biocurrent amplification like that for the wild-type (see Figure 10g). CV measurement traces confirmed that the COE-NDI/*S. oneidensis* MR-1 mutant complex has redox chemistry that can be explained by the LUMO energy levels of the COE-NDI, see Figure 10h. These experiments revealed the possibility of using COEs as membrane protein prosthetics for bioelectrosynthetic applications.

### 5.4. Perspectives on Interfacing CPEs and COEs in Bioelectrosynthetic Settings

As discussed in previous sections, the metabolic pathways of electrogenic bacteria can be coupled with materials technology to amplify electron transfer outside and within the *S. oneidensis* MR-1's membrane.[108,113] Bioelectrosynthetic amplification could also be achieved with n-type CPEs or n-type membrane-intercalating COE. However, in both cases, matching the LUMO energy levels with the MtrCAB protein complex of *S. oneidensis* MR-1 is a requirement.[28,133,134] A possible route for exploration in 3D conductive hydrogels is through bacterial engineering to optimize their electrogenicity and potentially tune their respiration redox potential. Additionally, introducing enzymatic biocatalysis into 3D conductive hydrogels for biocatalysis amplification is an area of opportunity. Evaluating the transcriptomic profile of the bacteria after participating in the bioelectrosynthesis to assess

gene expression and adaptation is also needed to aid bacteria genetic engineering.

A key finding in these studies was that the *S. oneidensis* MR-1 mutant strain lacking specific components of the MtrCAB construct restored biosynthetic function after COE-NDI was intercalated into its membrane, suggesting a membrane protein prosthetic function. Consequently, using n-type COEs as membrane protein prosthetics for bioelectrosynthesis in artificial systems is an underexplored area of opportunity. As with the 3D conductive hydrogels, interfacing membrane protein prosthetics with tailor-made enzymes for biocatalysis amplification presents a significant area of opportunity.

### ■ AUTHOR INFORMATION

#### Corresponding Author

**Ricardo Javier Vázquez** − *Department of Chemistry, Indiana University, Bloomington, Indiana 47405, United States;* orcid.org/0000-0003-3245-8123; Email: ricvazqu@iu.edu

#### Authors

**Sarah J. Cox-Vázquez** − *Department of Chemistry, Indiana University, Bloomington, Indiana 47405, United States;* orcid.org/0000-0001-9779-9493

**Batul Shakir** − *Department of Chemistry, Indiana University, Bloomington, Indiana 47405, United States*

**Oscar Medrano** − *Department of Chemistry, Indiana University, Bloomington, Indiana 47405, United States*

**Dhari Shah** − *Department of Chemistry, Indiana University, Bloomington, Indiana 47405, United States*

**Kingsley Bortey** − *Department of Chemistry, Indiana University, Bloomington, Indiana 47405, United States*

**Bidisha Biswas** − *Department of Chemistry, Indiana University, Bloomington, Indiana 47405, United States*

**Austin Tran** − *Department of Chemistry, Indiana University, Bloomington, Indiana 47405, United States*

**Crystal Tran** − *Department of Chemistry, Indiana University, Bloomington, Indiana 47405, United States*

Complete contact information is available at:
https://pubs.acs.org/10.1021/jacsau.4c00789

#### Notes

The authors declare no competing financial interest.

### ■ REFERENCES

(1) Zhang, Q.; Hu, W.; Sirringhaus, H.; Müllen, K. Recent Progress in Emerging Organic Semiconductors. *Adv. Mater.*. John Wiley and Sons Inc, 2022. DOI: 10.1002/adma.202108701.

(2) Vázquez, R. J.; Kim, H.; Kobilka, B. M.; Hale, B. J.; Jeffries-EL, M.; Zimmerman, P.; Goodson, T. Evaluating the Effect of Heteroatoms on the Photophysical Properties of Donor-Acceptor Conjugated Polymers Based on 2,6-Di(Thiophen-2-Yl)Benzo[1,2-b:4,5-B′]Difuran: Two-Photon Cross-Section and Ultrafast Time-Resolved Spectroscopy. *J. Phys. Chem. C* 2017, 121 (27), 14382−14392.

(3) Cai, Z.; Vázquez, R. J.; Zhao, D.; Li, L.; Lo, W.; Zhang, N.; Wu, Q.; Keller, B.; Eshun, A.; Abeyasinghe, N.; Banaszak-Holl, H.; Goodson, T.; Yu, L. Two Photon Absorption Study of Low-Bandgap, Fully Conjugated Perylene Diimide-Thienoacene-Perylene Diimide Ladder-Type Molecules. *Chem. Mater.* 2017, 29 (16), 6726−6732.

(4) Kim, H.; Keller, B.; Ho-Wu, R.; Abeyasinghe, N.; Vázquez, R. J.; Goodson, T.; Zimmerman, P. M. Enacting Two-Electron Transfer from a Double-Triplet State of Intramolecular Singlet Fission. *J. Am. Chem. Soc.* 2018, 140 (25), 7760−7763.

(5) Vázquez, R. J. R. J.; Kim, H.; Zimmerman, P. M. P. M.; Goodson, T. Using Ultra-Fast Spectroscopy to Probe the Excited State Dynamics of a Reported Highly Efficient Thermally Activated Delayed Fluorescence Chromophore. *J. Mater. Chem. C Mater.* **2019**, 7 (14), 4210−4221.

(6) Vázquez, R. J.; Yun, J. H.; Muthike, A. K.; Howell, M.; Kim, H.; Madu, I. K.; Kim, T.; Zimmerman, P.; Lee, J. Y.; Goodson, T., III New Direct Approach for Determining the Reverse Intersystem Crossing Rate in Organic Thermally Activated Delayed Fluorescent (TADF) Emitters. *J. Am. Chem. Soc.* **2020**, 142 (18), 8074−8079.

(7) Fisher, L.; Vázquez, R. J.; Howell, M.; Muthike, A. K.; Orr, M. E.; Jiang, H.; Dodgen, B.; Lee, D. R.; Lee, J. Y.; Zimmerman, P.; Goodson, T. Investigation of Thermally Activated Delayed Fluorescence in Donor-Acceptor Organic Emitters with Time-Resolved Absorption Spectroscopy. *Chem. Mater.* **2022**, 34 (5), 2161−2175.

(8) Uoyama, H.; Goushi, K.; Shizu, K.; Nomura, H.; Adachi, C. Highly Efficient Organic Light-Emitting Diodes from Delayed Fluorescence. *Nature* **2012**, 492 (7428), 234−238.

(9) Rivnay, J.; Inal, S.; Salleo, A.; Owens, R. M.; Berggren, M.; Malliaras, G. G. Organic Electrochemical Transistors. *Nat. Rev. Mater.* **2018**, 3 (2), 17086.

(10) Zeglio, E.; Inganäs, O. Active Materials for Organic Electrochemical Transistors. *Adv. Mater.* **2018**, 30 (44), 1−18.

(11) Liu, Y.; Lian, M.; Chen, W.; Chen, H. Recent Advances in Fabrication and Functions of Neuromorphic System Based on Organic Field Effect Transistor. *International Journal of Extreme Manufacturing.* Institute of Physics, 2024. DOI: 10.1088/2631-7990/ad1e25.

(12) Kim, M.-K.; Park, Y.; Kim, I.-J.; Lee, J.-S. Emerging Materials for Neuromorphic Devices and Systems. *iScience* **2020**, 23, 101846.

(13) Biswas, B.; Shah, D.; Cox-Vázquez, S. J.; Vázquez, R. J. Sensing Cholesterol-Induced Rigidity in Model Membranes with Time-Resolved Fluorescence Spectroscopy and Microscopy. *J. Mater. Chem. B* **2024**, 12, 6570.

(14) Zhou, C.; Cox-Vázquez, S. J.; Chia, G. W. N.; Vázquez, R. J.; Lai, H. Y.; Chan, S. J. W.; Limwongyut, J.; Bazan, G. C. Water-Soluble Extracellular Vesicle Probes Based on Conjugated Oligoelectrolytes. *Sci. Adv.* **2023**, 9 (2), 1−15.

(15) García-López, V.; Chen, F.; Nilewski, L. G.; Duret, G.; Aliyan, A.; Kolomeisky, A. B.; Robinson, J. T.; Wang, G.; Pal, R.; Tour, J. M. Molecular Machines Open Cell Membranes. *Nature* **2017**, 548 (7669), 567−572.

(16) Poizot, P.; Gaubicher, J.; Renault, S.; Dubois, L.; Liang, Y.; Yao, Y. Opportunities and Challenges for Organic Electrodes in Electrochemical Energy Storage. *Chemical Reviews* **2020**, 120, 6490−6557, DOI: 10.1021/acs.chemrev.9b00482.

(17) Schon, T. B.; McAllister, B. T.; Li, P. F.; Seferos, D. S. The Rise of Organic Electrode Materials for Energy Storage. *Chemical Society Reviews.* Royal Society of Chemistry, 2016; pp 6345−6404. DOI: 10.1039/c6cs00173d.

(18) Jiang, H.; Taranekar, P.; Reynolds, J. R.; Schanze, K. S. Conjugated Polyelectrolytes: Synthesis, Photophysics, and Applications. *Angewandte Chemie - International Edition.* **2009**, 48, 4300−4316.

(19) Lee, W.; Seo, J. H.; Woo, H. Y. Conjugated Polyelectrolytes: A New Class of Semiconducting Material for Organic Electronic Devices. *Polymer.*; Elsevier Ltd, 2013; pp 5104−5121. DOI: 10.1016/j.polymer.2013.07.015.

(20) Tan, C.; Wang, S.; Barboza-Ramos, I.; Schanze, K. S. A Perspective Looking Backward and Forward on the 25th Anniversary of Conjugated Polyelectrolytes. *ACS Applied Materials and Interfaces* **2024**, 16, 19887 DOI: 10.1021/acsami.4c02617.

(21) Wang, B.; Fronk, S. L.; Rengert, Z. D.; Limwongyut, J.; Bazan, G. C. Conjugated Oligoelectrolytes: Materials for Acceleration of Whole Cell Biocatalysis. *Chem. Mater.* **2018**, 30 (17), 5836−5840.

(22) Minudri, D.; Mantione, D.; Dominguez-Alfaro, A.; Moya, S.; Maza, E.; Bellacanzone, C.; Antognazza, M. R.; Mecerreyes, D. Water Soluble Cationic Poly(3,4-Ethylenedioxythiophene) PEDOT-N as a Versatile Conducting Polymer for Bioelectronics. *Adv. Electron Mater.* **2020**, 6 (10), 1−10.

(23) Tsokkou, D.; Peterhans, L.; Cao, D. X.; Mai, C. K.; Bazan, G. C.; Nguyen, T. Q.; Banerji, N. Excited State Dynamics of a Self-Doped Conjugated Polyelectrolyte. *Adv. Funct Mater.* **2020**, 30, 1906148 DOI: 10.1002/adfm.201906148.

(24) Mai, C. K.; Zhou, H.; Zhang, Y.; Henson, Z. B.; Nguyen, T. Q.; Heeger, A. J.; Bazan, G. C. Facile Doping of Anionic Narrow-Band-Gap Conjugated Polyelectrolytes during Dialysis. *Angewandte Chemie - International Edition* **2013**, 52 (49), 12874−12878.

(25) Wang, S.; Liu, B.; Gaylord, B. S.; Bazan, G. C. Size-Specific Interactions between Single- and Double-Stranded Oligonucleotides and Cationic Water-Soluble Oligofluorenes. *Adv. Funct Mater.* **2003**, 13 (6), 463−467.

(26) Zhou, C.; Chia, G. W. N.; Yong, K.-T. Membrane-Intercalating Conjugated Oligoelectrolytes. *Chem. Soc. Rev.* **2022**, 51 (24), 9917−9932.

(27) Zhou, C.; Li, Z.; Zhu, Z.; Chia, G. W. N.; Mikhailovsky, A.; Vázquez, R. J.; Chan, S. J. W.; Li, K.; Liu, B.; Bazan, G. C. Conjugated Oligoelectrolytes for Long-Term Tumor Tracking with Incremental NIR-II Emission. *Adv. Mater.* **2022**, 34 (20), 2201989.

(28) Quek, G.; Vázquez, R. J.; McCuskey, S. R.; Lopez-Garcia, F.; Bazan, G. C. An N-Type Conjugated Oligoelectrolyte Mimics Transmembrane Electron Transport Proteins for Enhanced Microbial Electrosynthesis. *Angew. Chem., Int. Ed.* **2023**, 62 (33). DOI: 10.1002/anie.202305189.

(29) Mahanta, C. S.; Ravichandiran, V.; Swain, S. P. Recent Developments in the Design of New Water-Soluble Boron Dipyrromethenes and Their Applications: An Updated Review. *ACS Applied Bio Materials* **2023**, 6, 2995−3018, DOI: 10.1021/acsabm.3c00289.

(30) Joshi, A.; Mukherjee, N.; Pandey, M. Water-Soluble Organic Fluorescence-Based Probes for Biomolecule Sensing and Labeling. *Biosensors and Bioelectronics: X.* Elsevier Ltd, 2024. DOI: 10.1016/j.biosx.2024.100510.

(31) Gao, Z.; Zhang, X.; Zheng, M.; Chen, Y. Synthesis of a Water Soluble Red Fluorescent Dye and Its Application to Living Cells Imaging. *Dyes Pigm.* **2015**, 120, 37−43.

(32) Yip, B. R. P.; Javier Vázquez, R.; Jiang, Y.; McCuskey, S. R.; Quek, G.; Ohayon, D.; Wang, X.; Bazan, G. C. Conjugated Polyelectrolyte Thin Films for Pseudocapacitive Applications. *Adv. Mater.* **2024**, 36 (1). DOI: 10.1002/adma.202308631.

(33) Vázquez, R. J.; Quek, G.; Jiang, Y.; Rui Peng, B. Y.; McCuskey, S. R.; Ohayon, D.; Kundukad, B.; Wang, X.; Bazan, G. C. Pseudocapacitive Gels Based on Conjugated Polyelectrolytes: Thickness and Ion Diffusion Limitations. *J. Mater. Chem. A Mater.* **2023**, 11 (35), 18843−18852.

(34) Tanwar, A. S.; Khatun, M. N.; Chanu, M. A.; Sarmah, T.; Im, Y.-H.; Iyer, P. K. A Water-Soluble Conjugated Polyelectrolyte for Selective and Sensitive Detection of Carcinogenic Chromium (VI). *Analyst* **2023**, 148 (23), 6011−6019.

(35) Ghosh, P.; Iyer, P. K. Conjugated Polyelectrolytes: Illuminating the Path to Neurodegenerative Disorders Detection and Treatment. *ACS Appl. Mater. Interfaces* **2024**, DOI: 10.1021/acsami.3c17890.

(36) Wang, Y.; Liu, Y. Insight into Conjugated Polymers for Organic Electrochemical Transistors. *Trends Chem.* **2023**, 5 (4), 279−294.

(37) Minudri, D.; Mantione, D.; Dominguez-Alfaro, A.; Moya, S.; Maza, E.; Bellacanzone, C.; Antognazza, M. R.; Mecerreyes, D. Water Soluble Cationic Poly(3,4-Ethylenedioxythiophene) PEDOT-N as a Versatile Conducting Polymer for Bioelectronics. *Adv. Electron Mater.* **2020**, 6 (10), 1−10.

(38) Hallani, R. K.; Paulsen, B. D.; Petty, A. J.; Sheelamanthula, R.; Moser, M.; Thorley, K. J.; Sohn, W.; Rashid, R. B.; Savva, A.; Moro, S.; Parker, J. P.; Drury, O.; Alsufyani, M.; Neophytou, M.; Kosco, J.; Inal, S.; Costantini, G.; Rivnay, J.; McCulloch, I. Regiochemistry-Driven Organic Electrochemical Transistor Performance Enhancement in Ethylene Glycol-Functionalized Polythiophenes. *J. Am. Chem. Soc.* **2021**, 143 (29), 11007−11018.

(39) Nie, G.; Yang, H.; Chen, J.; Bai, Z. A Novel High-Quality Electrochromic Material from 3,4- Ethylenedioxythiophene Bis-Substituted Fluorene. *Org. Electron* 2012, 13 (10), 2167−2176.

(40) Quek, G.; Roehrich, B.; Su, Y.; Sepunaru, L.; Bazan, G. C. Conjugated Polyelectrolytes: Underexplored Materials for Pseudocapacitive Energy Storage. *Adv. Mater.* 2022, 34 (22), 2104206.

(41) Wu, R.; Matta, M.; Paulsen, B. D.; Rivnay, J. Operando Characterization of Organic Mixed Ionic/Electronic Conducting Materials. *Chemical Reviews* 2022, 122, 4493−4551, DOI: 10.1021/acs.chemrev.1c00597.

(42) Lill, A. T.; Cao, D. X.; Schrock, M.; Vollbrecht, J.; Huang, J.; Nguyen-Dang, T.; Brus, V. V.; Yurash, B.; Leifert, D.; Bazan, G. C.; Nguyen, T.-Q. Organic Electrochemical Transistors Based on the Conjugated Polyelectrolyte PCPDTBT-SO3 K (CPE-K). *Adv. Mater.* 2020, 32 (33), No. e1908120.

(43) Chae, S.; Nguyen-Dang, T.; Chatsirisupachai, J.; Yi, A.; Vázquez, R. J.; Quek, G.; Promarak, V.; Kim, H. J.; Bazan, G. C.; Nguyen, T. Impact of Molecular Weight on the Ionic and Electronic Transport of Self-Doped Conjugated Polyelectrolytes Relevant to Organic Electrochemical Transistors. *Adv. Funct Mater.* 2024, 34 (3). DOI: 10.1002/adfm.202310852.

(44) Xia, F.; Zuo, X.; Yang, R.; Xiao, Y.; Kang, D.; Vallée-Bélisle, A.; Gong, X.; Yuen, J. D.; Hsu, B. B. Y.; Heeger, A. J.; Plaxco, K. W. Colorimetric Detection of DNA, Small Molecules, Proteins, and Ions Using Unmodified Gold Nanoparticles and Conjugated Polyelectrolytes. *Proc. Natl. Acad. Sci. U.S.A.* 2010, 107 (24), 10837−10841. .

(45) Paulsen, B. D.; Tybrandt, K.; Stavrinidou, E.; Rivnay, J. Organic Mixed Ionic-Electronic Conductors. *Nat. Mater.* 2020, 19 (1), 13−26.

(46) DUNCAN, R. R.; BERGMANN, A.; COUSIN, M. A.; APPS, D. K.; SHIPSTON, M. J. Multi-dimensional Time-correlated Single Photon Counting (TCSPC) Fluorescence Lifetime Imaging Microscopy (FLIM) to Detect FRET in Cells. *J. Microsc* 2004, 215 (1), 1−12.

(47) Zhao, M.; Huang, R.; Peng, L. Quantitative Multi-Color FRET Measurements by Fourier Lifetime Excitation-Emission Matrix Spectroscopy. *Opt. Express* 2012, 20, 26806.

(48) Klymchenko, A. S. Solvatochromic and Fluorogenic Dyes as Environment-Sensitive Probes: Design and Biological Applications. *Acc. Chem. Res.* 2017, 50 (2), 366−375.

(49) Garner, L. E.; Park, J.; Dyar, S. M.; Chworos, A.; Sumner, J. J.; Bazan, G. C. Modification of the Optoelectronic Properties of Membranes via Insertion of Amphiphilic Phenylenevinylene Oligoelectrolytes. *J. Am. Chem. Soc.* 2010, 132 (29), 10042−10052.

(50) Liu, B.; Gaylord, B. S.; Wang, S.; Bazan, G. C. Effect of Chromophore-Charge Distance on the Energy Transfer Properties of Water-Soluble Conjugated Oligomers. *J. Am. Chem. Soc.* 2003, 125 (22), 6705−6714.

(51) Gwozdzinska, P.; Pawlowska, R.; Milczarek, J.; Garner, L. E.; Thomas, A. W.; Bazan, G. C.; Chworos, A. Phenylenevinylene Conjugated Oligoelectrolytes as Fluorescent Dyes for Mammalian Cell Imaging. *Chem. Commun.* 2014, 50 (94), 14859−14861.

(52) Czernek, L.; Chworos, A.; Duechler, M. The Uptake of Extracellular Vesicles Is Affected by the Differentiation Status of Myeloid Cells. *Scand J. Immunol* 2015, 82 (6), 506−514.

(53) Zhou, C.; Chia, G. W. N.; Ho, J. C. S.; Moreland, A. S.; Seviour, T.; Liedberg, B.; Parikh, A. N.; Kjelleberg, S.; Hinks, J.; Bazan, G. C. A Chain-Elongated Oligophenylenevinylene Electrolyte Increases Microbial Membrane Stability. *Adv. Mater.* 2019, 31 (18). DOI: 10.1002/adma.201808021.

(54) Zhou, C.; Ho, J. C. S.; Chia, G. W. N.; Moreland, A. S.; Ruan, L.; Liedberg, B.; Kjelleberg, S.; Hinks, J.; Bazan, G. C. Gram-Typing Using Conjugated Oligoelectrolytes. *Adv. Funct Mater.* 2020, 30 (42). DOI: 10.1002/adfm.202004068.

(55) Zhu, J. Y.; Bazan, G. C. Molecular Orientation and Optimization of Membrane Dyes Based on Conjugated Oligoelectrolytes. *Cell Rep. Phys. Sci.* 2023, 4 (6), 101429.

(56) Zhu, J. Y.; Mikhailovsky, A.; Wei, S. C. J.; Moreland, A.; Limwongyut, J.; Guarrotxena, N.; Bazan, G. C. Photophysics of Conjugated Oligoelectrolytes Relevant to Two-Photon Fluorescence-

Lifetime Imaging Microscopy. *Adv. Funct Mater.* 2023, 33 (42). DOI: 10.1002/adfm.202305962.

(57) Veys, K.; Escudero, D. Anti-Kasha Fluorescence in Molecular Entities: Central Role of Electron-Vibrational Coupling. *Acc. Chem. Res.* 2022, 55 (18), 2698−2707.

(58) Tiihonen, A.; Cox-Vazquez, S. J.; Liang, Q.; Ragab, M.; Ren, Z.; Hartono, N. T. P.; Liu, Z.; Sun, S.; Zhou, C.; Incandela, N. C.; Limwongyut, J.; Moreland, A. S.; Jayavelu, S.; Bazan, G. C.; Buonassisi, T. Predicting Antimicrobial Activity of Conjugated Oligoelectrolyte Molecules via Machine Learning. *J. Am. Chem. Soc.* 2021, 143 (45), 18917−18931.

(59) Sareen, D.; Kaur, P.; Singh, K. Strategies in Detection of Metal Ions Using Dyes. *Coord. Chem. Rev.* 2014, 265, 125−154.

(60) Paez-Perez, M.; Vyšniauskas, A.; López-Duarte, I.; Lafarge, E. J.; López-Ríos De Castro, R.; Marques, C. M.; Schroder, A. P.; Muller, P.; Lorenz, C. D.; Brooks, N. J.; Kuimova, M. K. Directly Imaging Emergence of Phase Separation in Peroxidized Lipid Membranes. *Commun. Chem.* 2023, 6 (1). DOI: 10.1038/s42004-022-00809-x.

(61) Oliveira, E.; Bértolo, E.; Núñez, C.; Pilla, V.; Santos, H. M.; Fernández-Lodeiro, J.; Fernández-Lodeiro, A.; Djafari, J.; Capelo, J. L.; Lodeiro, C. Green and Red Fluorescent Dyes for Translational Applications in Imaging and Sensing Analytes: A Dual-Color Flag. *ChemistryOpen* 2018, 7 (1), 9−52.

(62) Sahoo, B. R.; Cox, S. J.; Ramamoorthy, A. High-Resolution Probing of Early Events in Amyloid-β Aggregation Related to Alzheimer's Disease. *Chem. Commun.* 2020, 56 (34), 4627−4639.

(63) Cox, S. J.; Lam, B.; Prasad, A.; Marietta, H. A.; Stander, N. V.; Joel, J. G.; Sahoo, B. R.; Guo, F.; Stoddard, A. K.; Ivanova, M. I.; Ramamoorthy, A. High-Throughput Screening at the Membrane Interface Reveals Inhibitors of Amyloid-β. *Biochemistry* 2020, 59 (24), 2249−2258.

(64) Fanni, A. M.; Monge, F. A.; Lin, C. Y.; Thapa, A.; Bhaskar, K.; Whitten, D. G.; Chi, E. Y. High Selectivity and Sensitivity of Oligomeric P-Phenylene Ethynylenes for Detecting Fibrillar and Prefibrillar Amyloid Protein Aggregates. *ACS Chemical Neuroscience* 2019, 10, 1813−1825, DOI: 10.1021/acschemneuro.8b00719.

(65) Monge, F. A.; Fanni, A. M.; Donabedian, P. L.; Hulse, J.; Maphis, N. M.; Jiang, S.; Donaldson, T. N.; Clark, B. J.; Whitten, D. G.; Bhaskar, K.; Chi, E. Y. Selective In Vitro and Ex Vivo Staining of Brain Neurofibrillary Tangles and Amyloid Plaques by Novel Ethylene Ethynylene-Based Optical Sensors. *Biosensors (Basel)* 2023, 13 (2), 151.

(66) Zielonka, J.; Joseph, J.; Sikora, A.; Hardy, M.; Ouari, O.; Vasquez-Vivar, J.; Cheng, G.; Lopez, M.; Kalyanaraman, B. Mitochondria-Targeted Triphenylphosphonium-Based Compounds: Syntheses, Mechanisms of Action, and Therapeutic and Diagnostic Applications. *Chem. Rev.* 2017, 117 (15), 10043−10120.

(67) Iaubasarova, I. R.; Khailova, L. S.; Firsov, A. M.; Grivennikova, V. G.; Kirsanov, R. S.; Korshunova, G. A.; Kotova, E. A.; Antonenko, Y. N. The Mitochondria-Targeted Derivative of the Classical Uncoupler of Oxidative Phosphorylation Carbonyl Cyanide m-Chlorophenylhydrazone Is an Effective Mitochondrial Recoupler. *PLoS One* 2020, 15 (12), No. e0244499.

(68) Chan, S. J. W.; Zhu, J. Y.; Mia Soh, W. W.; Bazan, G. C. Real-Time Monitoring of Mitochondrial Damage Using Conjugated Oligoelectrolytes. *J. Am. Chem. Soc.* 2024, 146 (1), 660−667.

(69) Chattopadhyay, P. K.; Gaylord, B.; Palmer, A.; Jiang, N.; Raven, M. A.; Lewis, G.; Reuter, M. A.; Nur-ur Rahman, A. K. M.; Price, D. A.; Betts, M. R.; Roederer, M. Brilliant Violet Fluorophores: A New Class of Ultrabright Fluorescent Compounds for Immunofluorescence Experiments. *Cytometry Part A* 2012, 81A (6), 456−466.

(70) Choi, N.-E.; Lee, J.-Y.; Park, E.-C.; Lee, J.-H.; Lee, J. Recent Advances in Organelle-Targeted Fluorescent Probes. *Molecules* 2021, 26 (1), 217.

(71) Xu, W.; Zeng, Z.; Jiang, J.; Chang, Y.; Yuan, L. Discerning the Chemistry in Individual Organelles with Small-Molecule Fluorescent Probes. *Angew. Chem., Int. Ed.* 2016, 55 (44), 13658−13699.

(72) Klymchenko, A. S. Fluorescent Probes for Lipid Membranes: From the Cell Surface to Organelles. *Acc. Chem. Res.* **2023**, *56* (1), 1−12.

(73) Gao, P.; Pan, W.; Li, N.; Tang, B. Fluorescent Probes for Organelle-Targeted Bioactive Species Imaging. *Chem. Sci.* **2019**, *10* (24), 6035−6071.

(74) Hinks, J.; Poh, W. H.; Hann Chu, J. J.; Chye Loo, J. S.; Bazan, G. C.; Hancock, L. E.; Wuertz, S. Oligopolyphenylenevinylene-Conjugated Oligoelectrolyte Membrane Insertion Molecules Selectively Disrupt Cell Envelopes of Gram-Positive Bacteria. *Appl. Environ. Microbiol.* **2015**, *81* (6), 1949−1958.

(75) Chan, S. J. W.; Zhu, J. Y.; Mia Soh, W. W.; Bazan, G. C. Real-Time Monitoring of Mitochondrial Damage Using Conjugated Oligoelectrolytes. *J. Am. Chem. Soc.* **2024**, *146*, 660.

(76) Llanes, L. C.; Lill, A. T.; Wan, Y.; Chae, S.; Yi, A.; Nguyen-Dang, T.; Kim, H. J.; Sepunaru, L.; Read de Alaniz, J.; Lu, G.; Bazan, G. C.; Nguyen, T.-Q. Side-Chain Engineering of Self-Doped Conjugated Polyelectrolytes for Organic Electrochemical Transistors. *J. Mater. Chem. C Mater.* **2023**, *11* (24), 8274−8283.

(77) Dimov, I. B.; Moser, M.; Malliaras, G. G.; McCulloch, I. Semiconducting Polymers for Neural Applications. *Chem. Rev.* **2022**, *122* (4), 4356−4396.

(78) Kousseff, C. J.; Halaksa, R.; Parr, Z. S.; Nielsen, C. B. Mixed Ionic and Electronic Conduction in Small-Molecule Semiconductors. *Chem. Rev.* **2022**, *122* (4), 4397−4419.

(79) Wu, R.; Paulsen, B. D.; Ma, Q.; Rivnay, J. Mass and Charge Transport Kinetics in an Organic Mixed Ionic-Electronic Conductor. *Chem. Mater.* **2022**, *34* (21), 9699−9710.

(80) Rivnay, J.; Leleux, P.; Ferro, M.; Sessolo, M.; Williamson, A.; Koutsouras, D. A.; Khodagholy, D.; Ramuz, M.; Strakosas, X.; Owens, R. M.; Benar, C.; Badier, J. M.; Bernard, C.; Malliaras, G. G. High-Performance Transistors for Bioelectronics through Tuning of Channel Thickness. *Sci. Adv.* **2015**, *1* (4), 1−6.

(81) Wang, J.; Lee, S.; Yokota, T.; Jimbo, Y.; Wang, Y.; Goni Nayeem, M. O.; Nishinaka, M.; Someya, T. Nanomesh Organic Electrochemical Transistor for Comfortable On-Skin Electrodes with Local Amplifying Function. *ACS Appl. Electron Mater.* **2020**, *2* (11), 3601−3609.

(82) Khodagholy, D.; Rivnay, J.; Sessolo, M.; Gurfinkel, M.; Leleux, P.; Jimison, L. H.; Stavrinidou, E.; Herve, T.; Sanaur, S.; Owens, R. M.; Malliaras, G. G. High Transconductance Organic Electrochemical Transistors. *Nat. Commun.* **2013**, *4*. DOI: 10.1038/ncomms3133.

(83) Nozella, N. L.; Lima, J. V. M.; de Oliveira, R. F.; de Oliveira Graeff, C. F. Melanin/PEDOT:PSS Blend as Organic Mixed Ionic Electronic Conductor (OMIEC) for Sustainable Electronics. *Mater. Adv.* **2023**, *4* (20), 4732−4743.

(84) Ohayon, D.; Druet, V.; Inal, S. A Guide for the Characterization of Organic Electrochemical Transistors and Channel Materials. *Chemical Society Reviews*. Royal Society of Chemistry, 2023; pp 1001−1023. DOI: 10.1039/d2cs00920j.

(85) Mai, C. K.; Zhou, H.; Zhang, Y.; Henson, Z. B.; Nguyen, T. Q.; Heeger, A. J.; Bazan, G. C. Facile Doping of Anionic Narrow-Band-Gap Conjugated Polyelectrolytes during Dialysis. *Angewandte Chemie - International Edition* **2013**, *52* (49), 12874−12878.

(86) De Sio, A.; Troiani, F.; Maiuri, M.; Réhault, J.; Sommer, E.; Lim, J.; Huelga, S. F.; Plenio, M. B.; Rozzi, C. A.; Cerullo, G.; Molinari, E.; Lienau, C. Tracking the Coherent Generation of Polaron Pairs in Conjugated Polymers. *Nat. Commun.* **2016**, *7*. DOI: 10.1038/ncomms13742.

(87) Schmode, P.; Ohayon, D.; Reichstein, P. M.; Savva, A.; Inal, S.; Thelakkat, M. High-Performance Organic Electrochemical Transistors Based on Conjugated Polyelectrolyte Copolymers. *Chem. Mater.* **2019**, *31* (14), 5286−5295.

(88) Håkansson, A.; Han, S.; Wang, S.; Lu, J.; Braun, S.; Fahlman, M.; Berggren, M.; Crispin, X.; Fabiano, S. Effect of (3-Glycidyloxypropyl)Trimethoxysilane (GOPS) on the Electrical Properties of PEDOT:PSS Films. *J. Polym. Sci. B Polym. Phys.* **2017**, *55* (10), 814−820.

(89) Kim, S. M.; Kim, C. H.; Kim, Y.; Kim, N.; Lee, W. J.; Lee, E. H.; Kim, D.; Park, S.; Lee, K.; Rivnay, J.; Yoon, M. H. Influence of PEDOT:PSS Crystallinity and Composition on Electrochemical Transistor Performance and Long-Term Stability. *Nat. Commun.* **2018**, *9* (1). DOI: 10.1038/s41467-018-06084-6.

(90) Taussig, L.; Ghasemi, M.; Han, S.; Kwansa, A. L.; Li, R.; Keene, S. T.; Woodward, N.; Yingling, Y. G.; Malliaras, G. G.; Gomez, E. D.; Amassian, A. Electrostatic Self-Assembly Yields a Structurally Stabilized PEDOT:PSS with Efficient Mixed Transport and High-Performance OECTs. *Matter* **2024**, *7* (3), 1071−1091.

(91) Llanes, L. C.; Lill, A. T.; Wan, Y.; Chae, S.; Yi, A.; Nguyen-Dang, T.; Kim, H. J.; Sepunaru, L.; Read de Alaniz, J.; Lu, G.; Bazan, G. C.; Nguyen, T. Q. Side-Chain Engineering of Self-Doped Conjugated Polyelectrolytes for Organic Electrochemical Transistors. *J. Mater. Chem. C Mater.* **2023**, *11* (24), 8274−8283.

(92) Jiang, Y.; Vázquez, R. J.; McCuskey, S. R.; Yip, B. R. P.; Quek, G.; Ohayon, D.; Kundukad, B.; Wang, X.; Bazan, G. C. Recyclable Conjugated Polyelectrolyte Hydrogels for Pseudocapacitor Fabrication. *ACS Appl. Mater. Interfaces* **2023**, DOI: 10.1021/acsami.3c13137.

(93) Nguyen-Dang, T.; Chae, S.; Chatsirisupachai, J.; Wakidi, H.; Promarak, V.; Visell, Y.; Nguyen, T. Q. Dual-Mode Organic Electrochemical Transistors Based on Self-Doped Conjugated Polyelectrolytes for Reconfigurable Electronics. *Adv. Mater.* **2022**, *34* (23). DOI: 10.1002/adma.202200274.

(94) Giovannitti, A.; Nielsen, C. B.; Sbircea, D.-T.; Inal, S.; Donahue, M.; Niazi, M. R.; Hanifi, D. A.; Amassian, A.; Malliaras, G. G.; Rivnay, J.; McCulloch, I. N-Type Organic Electrochemical Transistors with Stability in Water. *Nat. Commun.* **2016**, *7* (1), 13066.

(95) Ahmed, H. T.; Jalal, V. J.; Tahir, D. A.; Mohamad, A. H.; Abdullah, O. G. Effect of PEG as a Plasticizer on the Electrical and Optical Properties of Polymer Blend Electrolyte MC-CH-LiBF4 Based Films. *Results Phys.* **2019**, *15*, 102735.

(96) Maria, I. P.; Paulsen, B. D.; Savva, A.; Ohayon, D.; Wu, R.; Hallani, R.; Basu, A.; Du, W.; Anthopoulos, T. D.; Inal, S.; Rivnay, J.; McCulloch, I.; Giovannitti, A. The Effect of Alkyl Spacers on the Mixed Ionic-Electronic Conduction Properties of N-Type Polymers. *Adv. Funct Mater.* **2021**, *31* (14). DOI: 10.1002/adfm.202008718.

(97) Giovannitti, A.; Maria, I. P.; Hanifi, D.; Donahue, M. J.; Bryant, D.; Barth, K. J.; Makdah, B. E.; Savva, A.; Moia, D.; Zetek, M.; Barnes, P. R. F.; Reid, O. G.; Inal, S.; Rumbles, G.; Malliaras, G. G.; Nelson, J.; Rivnay, J.; McCulloch, I. The Role of the Side Chain on the Performance of N-Type Conjugated Polymers in Aqueous Electrolytes. *Chem. Mater.* **2018**, *30* (9), 2945−2953.

(98) Hungenberg, J.; Hochgesang, A.; Meichsner, F.; Thelakkat, M. Self-Doped Mixed Ionic-Electronic Conductors to Tune the Threshold Voltage and the Mode of Operation in Organic Electrochemical Transistors. *Adv. Funct Mater.* **2024**, DOI: 10.1002/adfm.202407067.

(99) Zeglio, E.; Vagin, M.; Musumeci, C.; Ajjan, F. N.; Gabrielsson, R.; Trinh, X. T.; Son, N. T.; Maziz, A.; Solin, N.; Inganäs, O. Conjugated Polyelectrolyte Blends for Electrochromic and Electrochemical Transistor Devices. *Chem. Mater.* **2015**, *27* (18), 6385−6393.

(100) Zeglio, E.; Eriksson, J.; Gabrielsson, R.; Solin, N.; Inganäs, O. Highly Stable Conjugated Polyelectrolytes for Water-Based Hybrid Mode Electrochemical Transistors. *Adv. Mater.* **2019**, *31* (5). DOI: 10.1002/adma.201807393.

(101) Sun, H.; Zhu, J.; Baumann, D.; Peng, L.; Xu, Y.; Shakir, I.; Huang, Y.; Duan, X. Hierarchical 3D Electrodes for Electrochemical Energy Storage. *Nature Reviews Materials*. Nature Publishing Group, 2019; pp 45−60. DOI: 10.1038/s41578-018-0069-9.

(102) Yang, Z.; Zhang, J.; Kintner-Meyer, M. C. W.; Lu, X.; Choi, D.; Lemmon, J. P.; Liu, J. Electrochemical Energy Storage for Green Grid. *Chem. Rev.* **2011**, *111* (5), 3577−3613.

(103) Beyers, I.; Bensmann, A.; Hanke-Rauschenbach, R. Ragone Plots Revisited: A Review of Methodology and Application across Energy Storage Technologies. *Journal of Energy Storage*. Elsevier Ltd, 2023. DOI: 10.1016/j.est.2023.109097.

(104) Fleischmann, S.; Mitchell, J. B.; Wang, R.; Zhan, C.; Jiang, D.; Presser, V.; Augustyn, V. Pseudocapacitance: From Fundamental Understanding to High Power Energy Storage Materials. *Chem. Rev.* **2020**, *120* (14), 6738−6782.

(105) Sahalianov, I.; Singh, S. K.; Tybrandt, K.; Berggren, M.; Zozoulenko, I. The Intrinsic Volumetric Capacitance of Conducting Polymers: Pseudo-Capacitors or Double-Layer Supercapacitors? *RSC Adv.* **2019**, *9* (72), 42498−42508.

(106) Mathis, T. S.; Kurra, N.; Wang, X.; Pinto, D.; Simon, P.; Gogotsi, Y. Energy Storage Data Reporting in Perspective— Guidelines for Interpreting the Performance of Electrochemical Energy Storage Systems. *Adv. Energy Mater.* **2019**, *9* (39), 1902007.

(107) Wang, X.; Bak, S.-M.; Han, M.; Shuck, C. E.; McHugh, C.; Li, K.; Li, J.; Tang, J.; Gogotsi, Y. Surface Redox Pseudocapacitance of Partially Oxidized Titanium Carbide MXene in Water-in-Salt Electrolyte. *ACS Energy Lett.* **2022**, *7* (1), 30−35.

(108) Logan, B. E. Exoelectrogenic Bacteria That Power Microbial Fuel Cells. *Nat. Rev. Microbiol* **2009**, *7* (5), 375−381.

(109) Logan, B. E.; Rabaey, K. Conversion of Wastes into Bioelectricity and Chemicals by Using Microbial Electrochemical Technologies. *Science (1979)* **2012**, *337* (6095), 686−690.

(110) McCuskey, S. R.; Chatsirisupachai, J.; Zeglio, E.; Parlak, O.; Panoy, P.; Herland, A.; Bazan, G. C.; Nguyen, T.-Q. Current Progress of Interfacing Organic Semiconducting Materials with Bacteria. *Chem. Rev.* **2022**, *122* (4), 4791−4825.

(111) Choudhury, P.; Bhunia, B.; Bandyopadhyay, T. K.; Ray, R. N. The Overall Performance Improvement of Microbial Fuel Cells Connected in Series with Dairy Wastewater Treatment. *Journal of Electrochemical Science and Technology* **2021**, *12* (1), 101−111.

(112) Sarkar, S.; Thangadurai, V. Critical Current Densities for High-Performance All-Solid-State Li-Metal Batteries: Fundamentals, Mechanisms, Interfaces, Materials, and Applications. *ACS Energy Lett.* **2022**, *7* (4), 1492−1527.

(113) McCuskey, S. R.; Su, Y.; Leifert, D.; Moreland, A. S.; Bazan, G. C. Living Bioelectrochemical Composites. *Adv. Mater.* **2020**, *32* (24), 1908178.

(114) Vázquez, R. J.; McCuskey, S. R.; Quek, G.; Su, Y.; Llanes, L.; Hinks, J.; Bazan, G. C. Conjugated Polyelectrolyte/Bacteria Living Composites in Carbon Paper for Biocurrent Generation. *Macromol. Rapid Commun.* **2022**, *43* (16), 2100840.

(115) Song, R.-B.; Wu, Y.; Lin, Z.-Q.; Xie, J.; Tan, C. H.; Loo, J. S. C.; Cao, B.; Zhang, J.-R.; Zhu, J.-J.; Zhang, Q. Living and Conducting: Coating Individual Bacterial Cells with In Situ Formed Polypyrrole. *Angew. Chem.* **2017**, *129* (35), 10652−10656.

(116) Hu, Y.; Rehnlund, D.; Klein, E.; Gescher, J.; Niemeyer, C. M. Cultivation of Exoelectrogenic Bacteria in Conductive DNA Nanocomposite Hydrogels Yields a Programmable Biohybrid Materials System. *ACS Appl. Mater. Interfaces* **2020**, *12* (13), 14806−14813.

(117) Kirchhofer, N. D.; McCuskey, S. R.; Mai, C.-K.; Bazan, G. C. Anaerobic Respiration on Self-Doped Conjugated Polyelectrolytes: Impact of Chemical Structure. *Angew. Chem.* **2017**, *129* (23), 6619−6622.

(118) Marsili, E.; Baron, D. B.; Shikhare, I. D.; Coursolle, D.; Gralnick, J. A.; Bond, D. R. Shewanella Secretes Flavins That Mediate Extracellular Electron Transfer. *Proc. Natl. Acad. Sci. U. S. A.* **2008**, *105* (10), 3968−3973.

(119) Kirchhofer, N. D.; Chen, X.; Marsili, E.; Sumner, J. J.; Dahlquist, F. W.; Bazan, G. C. The Conjugated Oligoelectrolyte DSSN+ Enables Exceptional Coulombic Efficiency via Direct Electron Transfer for Anode-Respiring Shewanella Oneidensis MR-1—a Mechanistic Study. *Phys. Chem. Chem. Phys.* **2014**, *16* (38), 20436−20443.

(120) Su, Y.; McCuskey, S. R.; Leifert, D.; Moreland, A. S.; Zhou, L.; Llanes, L. C.; Vazquez, R. J.; Sepunaru, L.; Bazan, G. C. A Living Biotic-Abiotic Composite That Can Switch Function Between Current Generation and Electrochemical Energy Storage. *Adv. Funct Mater.* **2021**, *31* (6), 2007351.

(121) Zhang, K.; Feng, Q.; Xu, J.; Xu, X.; Tian, F.; Yeung, K. W. K.; Bian, L. Self-Assembled Injectable Nanocomposite Hydrogels Stabilized by Bisphosphonate-Magnesium (Mg2+) Coordination Regulates the Differentiation of Encapsulated Stem Cells via Dual Crosslinking. *Adv. Funct Mater.* **2017**, *27* (34), 1−11.

(122) Sheng, T.; Guan, X.; Liu, C.; Su, Y. De Novo Approach to Encapsulating Biocatalysts into Synthetic Matrixes: From Enzymes to Microbial Electrocatalysts. *ACS Appl. Mater. Interfaces* **2021**, *13* (44), 52234−52249.

(123) Xie, X.; Ye, M.; Hu, L.; Liu, N.; McDonough, J. R.; Chen, W.; Alshareef, H. N.; Criddle, C. S.; Cui, Y. Carbon Nanotube-Coated Macroporous Sponge for Microbial Fuel Cell Electrodes. *Energy Environ. Sci.* **2012**, *5* (1), 5265−5270.

(124) Li, S.; Cheng, C.; Thomas, A. Carbon-Based Microbial-Fuel-Cell Electrodes: From Conductive Supports to Active Catalysts. *Adv. Mater.* **2017**, *29* (8). DOI: 10.1002/adma.201602547.

(125) Quek, G.; Su, Y.; Donato, R. K.; Vázquez, R. J.; Marangoni, V. S.; Ng, P. R.; Costa, M. C. F.; Kundukad, B.; Novoselov, K. S.; Neto, A. H. C.; Bazan, G. C. Pseudocapacitive Conjugated Polyelectrolyte/ 2D Electrolyte Hydrogels with Enhanced Physico-Electrochemical Properties. *Adv. Electron Mater.* **2022**, *8* (5), 2100942.

(126) Vázquez, R. J.; Quek, G.; McCuskey, S. R.; Llanes, L.; Kundukad, B.; Wang, X.; Bazan, G. C. Increasing the Molecular Weight of Conjugated Polyelectrolytes Improves the Electrochemical Stability of Their Pseudocapacitor Gels. *J. Mater. Chem. A Mater.* **2022**, *10* (40), 21642−21649.

(127) Han, A.; Colby, R. H. Rheology of Entangled Polyelectrolyte Solutions. *Macromolecules* **2021**, *54* (3), 1375−1387.

(128) Maestro, A.; Ortega, F.; Monroy, F.; Krägel, J.; Miller, R. Molecular Weight Dependence of the Shear Rheology of Poly (Methyl Methacrylate) Langmuir Films: A Comparison between Two Different Rheometry Techniques. *Langmuir* **2009**, *25* (13), 7393−7400.

(129) Logan, B. E.; Rossi, R.; Ragab, A.; Saikaly, P. E. Electroactive Microorganisms in Bioelectrochemical Systems. *Nature Reviews Microbiology*. Nature Publishing Group, 2019; pp 307−319. DOI: 10.1038/s41579-019-0173-x.

(130) Finkelstein, J.; Swartz, J.; Koffas, M. Bioelectrosynthesis Systems. *Current Opinion in Biotechnology*. Elsevier Ltd, 2022; pp 211−219. DOI: 10.1016/j.copbio.2021.11.011.

(131) Mondal, D.; Fisher, B. F.; Jiang, Y.; Lewis, J. C. Flavin-Dependent Halogenases Catalyze Enantioselective Olefin Halocyclization. *Nat. Commun.* **2021**, *12* (1). DOI: 10.1038/s41467-021-23503-3.

(132) Paquete, C. M.; Saraiva, I. H.; Louro, R. O. Redox Tuning of the Catalytic Activity of Soluble Fumarate Reductases from Shewanella. *Biochim Biophys Acta Bioenerg* **2014**, *1837* (6), 717−725.

(133) Quek, G.; Vázquez, R. J.; McCuskey, S. R.; Kundukad, B.; Bazan, G. C. Enabling Electron Injection for Microbial Electrosynthesis with N-Type Conjugated Polyelectrolytes. *Adv. Mater.* **2022**, *34*, 2203480.

(134) Edwards, M. J.; White, G. F.; Butt, J. N.; Richardson, D. J.; Clarke, T. A. The Crystal Structure of a Biological Insulated Transmembrane Molecular Wire. *Cell* **2020**, *181* (3), 665−673.